

# Structural Diversity Design, Four Nucleation Methods Growth and Mechanism of 3D Hollow Box TiO<sub>2</sub> Nanocrystals with a Temperature-Controlled High (001) Crystal Facets Exposure Ratio

Shengqiang Liao, Huan Liu, Yanfei Lu, Chenglong Tang, Benjun Xi, and Lianqing Chen\*



Cite This: *ACS Omega* 2024, 9, 1695–1713



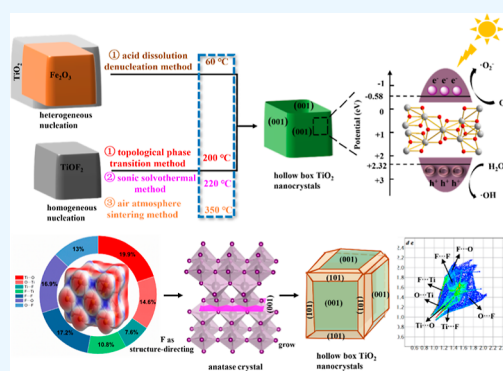
Read Online

ACCESS |

Metrics & More

Article Recommendations

**ABSTRACT:** Three-dimensional (3D) hollow box TiO<sub>2</sub> nanocrystals with structural diversity have been designed and grown by four nucleation methods, including the acid dissolution denucleation method with Fe<sub>2</sub>O<sub>3</sub> as heterogeneous nucleation, the topological phase transition method, the sonic solvothermal method, and the air atmosphere sintering method with TiOF<sub>2</sub> as homogeneous nucleation. Through full morphology analysis and structural characterization, reasonable growth mechanisms of 3D hollow box TiO<sub>2</sub> nanocrystals were proposed, including nucleation dissolution, Oswald ripening, and hydrolysis reactions. It was found that the high energy (001) crystal facets exposure ratio was closely correlated with reaction temperature of four nucleation-methods, which even reached 92% for the first time. Under simulated sunlight irradiation, their hydrogen production performance and photocatalytic degradation efficiency on model dye molecules rhodamine B (RhB) and methylene blue (MB) were evaluated, and as-prepared hollow box TiO<sub>2</sub> nanocrystals prepared by the sonic solvothermal method exhibited the best photocatalytic performance, with a hydrogen production rate of 93.88 μmol/g/h. Within 70 min, the photocatalytic degradation rates of RhB and MB reached 96.59 and 75.25%, respectively, which were 5.74 and 5.54 times that of P25. Their properties are closely connected with the orderly cubic and hierarchy configuration structure of hollow box TiO<sub>2</sub> nanocrystals, which have a high exposure ratio of (001) facet controlled by reaction temperatures, thereby greatly improving the photocatalytic activity. This study provides a classic reference for improving the properties of hollow box TiO<sub>2</sub> nanocrystals through structural diversity design and various methods of nanocrystal growth.



## 1. INTRODUCTION

In recent years, semiconductor nanocrystals have attracted increasingly more interest among researchers.<sup>1</sup> Semiconductor nanocrystals exhibit unique optical properties due to their small size, making them widely applicable in optical research.<sup>2,3</sup> Tuning the growth and shape evolution of specific crystal facets of semiconductor nanocrystals can enhance their optical characteristics.<sup>4,5</sup> Compared to bulk semiconductors, atoms, and molecules, the ultrasmall size of semiconductor nanocrystals alters the energy levels of the conduction and valence bands.<sup>6,7</sup> The degeneracy of the band edge states also increases, leading to quantization of nearby states. Additionally, due to their high surface area-to-volume ratio and surface-active sites, semiconductor nanocrystals often exhibit outstanding performance in catalysis and chemical reactions.<sup>7,8</sup> Therefore, designing semiconductor nanocrystals with appropriate dimensions and specific facet growth is of paramount importance.

Photocatalysis is a commonly used method to address environmental pollution and energy scarcity issues. TiO<sub>2</sub> is the most widely used photocatalytic material due to its high

chemical stability,<sup>9,10</sup> high degree of commercialization,<sup>11,12</sup> and excellent catalytic performance.<sup>13,14</sup> However, TiO<sub>2</sub> has low solar energy utilization and a high electron–hole recombination rate, indicating that the catalytic performance of TiO<sub>2</sub> still needs to be improved. Generally, anatase TiO<sub>2</sub> has better photocatalytic activity.<sup>15–17</sup> Zhu et al. used TiCl<sub>4</sub> and benzyl alcohol to carry out a nonhydrolytic sol–gel reaction at low temperature to prepare anatase TiO<sub>2</sub> nanoparticles, which have a much higher degradation effect on phenol than P25.<sup>18</sup> Changing the morphology of TiO<sub>2</sub> can improve its catalytic performance. Many special nanostructured TiO<sub>2</sub> materials have been developed, such as nanosheets,<sup>19</sup> nanowire,<sup>20</sup> nanotubes,<sup>21</sup> nanorods,<sup>22</sup> hollow nanoboxes,<sup>23</sup> and so on. Wang et al. prepared TiO<sub>2</sub> nanosheets with surfaces containing

**Received:** October 22, 2023

**Revised:** December 1, 2023

**Accepted:** December 6, 2023

**Published:** December 28, 2023



fluoride ions and oxygen vacancies, which showed excellent performance in the photocatalytic degradation of volatile organic compounds.<sup>24</sup> Horváth et al. prepared TiO<sub>2</sub> nanowire/nanotube composites, which can effectively remove various organic compounds and infectious microorganisms under sunlight.<sup>25</sup> So far, experimental and theoretical analyses have shown that the high-energy (001) facet of anatase TiO<sub>2</sub> can effectively separate photogenerated electron–hole pairs and improve photocatalytic ability. The research of Yang et al. shows that the average facet energy of anatase TiO<sub>2</sub> dioxide follows the order (001) with 0.90 J/m<sup>2</sup> > (100) with 0.53 J/m<sup>2</sup> > (101) with 0.44 J/m<sup>2</sup>. By constructing a layered, three-dimensional hollow nanobox of TiO<sub>2</sub> composed of six highly exposed (001) facets, the light response can be enhanced.<sup>26</sup>

Hollow nanobox TiO<sub>2</sub> possesses characteristics such as low density,<sup>27</sup> good surface permeability,<sup>28</sup> and a large surface area,<sup>29</sup> which contribute to their strong adsorption capacity.<sup>30</sup> Additionally, the hierarchical structure of hollow nanobox TiO<sub>2</sub> can generate multilevel scattering of light, where multiple scattering particles exist within the scattering body and each particle's scattered light can be rescattered by other particles. This leads to an increasing capture of light, effectively enhancing the utilization of light and thus enhancing the photocatalytic activity of TiO<sub>2</sub>.<sup>31</sup> Liu et al. used a simple self-template solvothermal annealing method to prepare novel double-shell ZnFe<sub>2</sub>O<sub>4</sub> hollow microspheres, and the kinetic constants of double-shell ZnFe<sub>2</sub>O<sub>4</sub> hollow spheres were 1.46 and 1.82 times those of the yolk–shell spheres and solid spheres, respectively. This indicates that the multishell hollow structure can adjust the refractive index, which is beneficial for enhancing light scattering.<sup>32</sup> Methods for preparing hollow nanobox TiO<sub>2</sub> include hydrothermal synthesis, cation-assisted methods, and so on. Zhang et al. used a one-pot method to prepare a Ti<sup>3+</sup>-doped three-dimensional TiO<sub>2</sub> hollow nanobox, which enhanced visible light response.<sup>33</sup> Li et al. prepared a hollow TiO<sub>2</sub> nanobox with enhanced electrochemical activity using a hydrothermal method and exhibited excellent electrochemical effects in electrochemical suspensions, contributing to improved dielectric performance.<sup>34</sup> However, there is limited research on hollow box TiO<sub>2</sub> nanocrystals. In order to obtain the optimal method for growing hollow box TiO<sub>2</sub> nanocrystals, four nucleation methods have been applied, including the acid dissolution denucleation method with Fe<sub>2</sub>O<sub>3</sub> as heterogeneous nucleation, the topological phase transition method, the sonic solvothermal method, and the air atmosphere sintering method with TiOF<sub>2</sub> as homogeneous nucleation.

The crystallization process is divided into two stages: nucleation and growth. Nucleation is the first step in crystal growth, where small crystals form in a solution. Once nuclei are formed, crystals grow by absorbing material from the solution, gas, or melt.<sup>35</sup> During the crystal growth process, heterogeneous nucleation or homogeneous nucleation is crucial.<sup>36</sup> In heterogeneous nucleation, the formation of crystals does not begin with free molecules in the solution but rather with heterogeneous nuclei.<sup>37</sup> In homogeneous nucleation, crystal formation originates from free ions, atoms, or molecules in the solution, and these molecules aggregate to form small nuclei.<sup>38</sup>

The acid-dissolution denucleation method is a typical heterogeneous nucleation approach. This method can replicate the micronanostructure of nucleation materials, construct the morphology of synthetic materials,<sup>39,40</sup> and precisely control

the size and arrangement of nanocrystals,<sup>41,42</sup> which has advantages such as simple operation, mild reaction conditions, and high efficiency in preparing zero-dimensional and one-dimensional nanomaterials. Yang et al. used wood as heterogeneous nucleation to prepare TiO<sub>2</sub> with a multilayered porous structure, achieving a degradation efficiency of 97.9% for methylene blue within 60 min.<sup>43</sup>

The topological phase transition method, the sonic solvothermal method, and the air atmosphere sintering method are three important homogeneous nucleation methods. The topological phase transition method and sonic solvothermal method can control the formation of phases, particle size, and shape, resulting in products with good dispersibility.<sup>44</sup> The topological phase transition process is typically conducted in a closed system. During the reaction process, the reactants dissolve and disperse in the solution, facilitating the progress of the reaction.<sup>45</sup> Jia et al. prepared layered TiO<sub>2-x</sub> hollow nanoboxes through the in situ topological phase transition solvent thermal method using peroxide.<sup>46</sup> The air atmosphere sintering method is primarily used for the manufacturing of ceramics, crystal conversion, separation, and enrichment. Sintering can alleviate the inherent tension in the molecular structure of substances, allowing them to adapt to increasing forces during the shaping process and become more robust upon completion.<sup>47,48</sup> When the sintering temperature reaches 500 °C, the anatase phase gradually transforms into the rutile phase, which exhibits lower catalytic activity compared to the anatase phase.<sup>49–51</sup> Compared to hollow box TiO<sub>2</sub> prepared by traditional methods, the hollow box TiO<sub>2</sub> nanocrystals prepared in this study have a higher (001) facet exposure ratio.

Herein, 3D hollow box TiO<sub>2</sub> nanocrystals were attempted to grow using one heterogeneous nucleation method and three homogeneous nucleation methods. Comprehensive morphological analysis, structural characterization, and growth mechanisms of hollow box TiO<sub>2</sub> nanocrystals by four methods were conducted and proposed. Furthermore, the evolution of the formation process and exposure rate of (001) crystal facets of hollow box TiO<sub>2</sub> nanocrystals was studied, and the impact of temperature on the (001) facet exposure rate was investigated. Finally, the photocatalytic performance of the hollow box TiO<sub>2</sub> nanocrystals was compared through photocatalytic hydrogen production and the degradation of RhB and MB. This research provides hollow box TiO<sub>2</sub> nanocrystals through structural diversity design and various methods of nanocrystal growth.

## 2. EXPERIMENTAL SECTION

**2.1. Materials.** Ferric chloride hexahydrate (FeCl<sub>3</sub>·6H<sub>2</sub>O), sodium hydroxide (NaOH), sodium carbonate (Na<sub>2</sub>CO<sub>3</sub>), titanium tetra-*n*-butylate [Ti(OC<sub>4</sub>H<sub>9</sub>)<sub>4</sub>], anhydrous ethanol (CH<sub>3</sub>CH<sub>2</sub>OH), hydrochloric acid (HCl), acetic acid (CH<sub>3</sub>COOH), hydrofluoric acid (HF), coumarin (C<sub>9</sub>H<sub>6</sub>O<sub>2</sub>), 4-chloro-7-nitro-2,1,3-benzoxadiazole (C<sub>6</sub>H<sub>2</sub>ClN<sub>3</sub>O<sub>3</sub>, NBD-Cl), silver nitrate (AgNO<sub>3</sub>), isopropanol (C<sub>3</sub>H<sub>8</sub>O), benzoquinone (C<sub>6</sub>H<sub>4</sub>O<sub>2</sub>), rhodamine B (C<sub>28</sub>H<sub>31</sub>ClN<sub>2</sub>O<sub>3</sub>, RhB), and methylene blue (C<sub>16</sub>H<sub>18</sub>N<sub>3</sub>ClS, MB) sourced from China National Pharmaceutical Group Chemical Reagent Co., Ltd. All materials are analytical grade and can be used directly without the need for further purification. Deionized water is used in all experiments.

**2.2. Hollow Box TiO<sub>2</sub> Nanocrystals Grown by the Heterogeneous Nucleation Method.** **2.2.1. Acid Dissolution Denucleation Method.** Under stirring, 25.0 g of FeCl<sub>3</sub>·6H<sub>2</sub>O was added to 50.0 mL of deionized water until fully

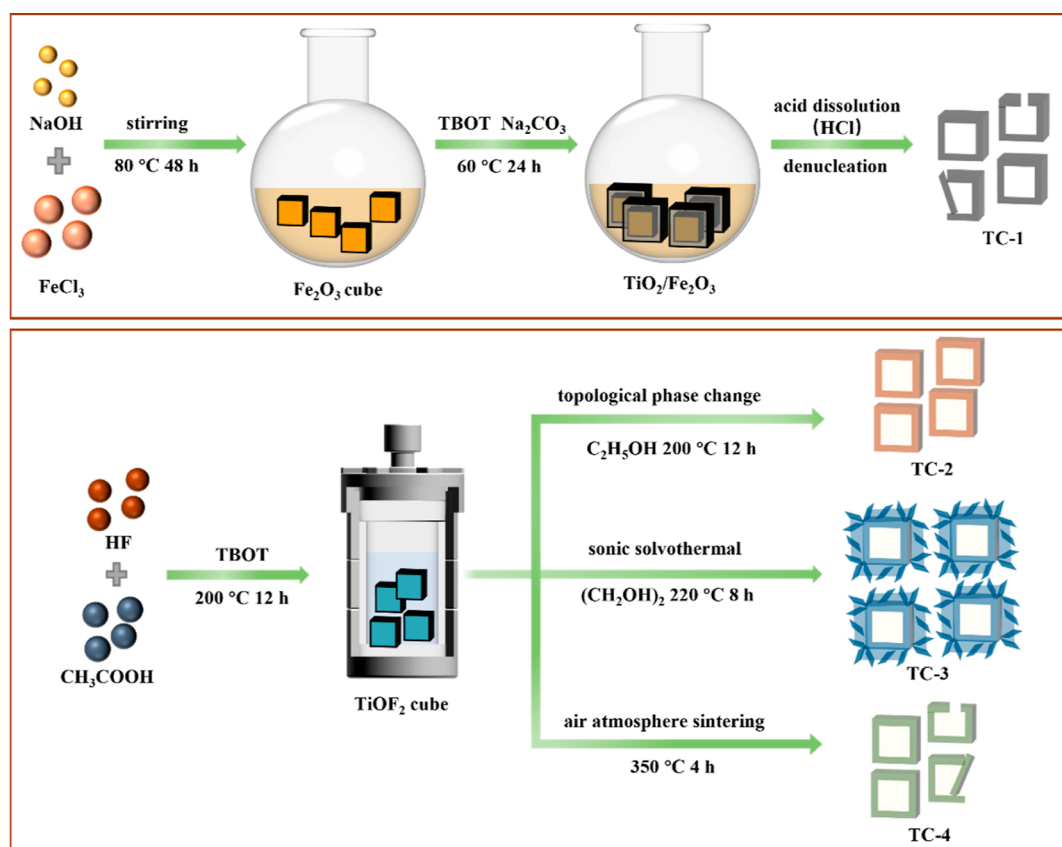


**Figure 1.** Growth of hollow box  $\text{TiO}_2$  nanocrystals by four nucleation methods.

dissolved. The solution was heated to 80 °C, then 50.0 mL of NaOH solution (5 M) was slowly added while stirring and reacted for 48 h. The precipitate was centrifuged to separate, washed with water and ethanol (3 times), and dried overnight at 60 °C. In 100.0 mL of ethanol, 0.4 mL of sodium carbonate solution (35 wt %) and the prepared nano  $\text{Fe}_2\text{O}_3$  (0.2 g) were added. The mixture was ultrasonicated for 15 min. After adding 1.0 mL of tetrabutyl titanate (TBOT), the mixture was stirred at 60 °C for 24 h. To separate the product, it was centrifuged, washed with ethanol (3 times), and dried overnight at 60 °C. The prepared  $\text{Fe}_2\text{O}_3/\text{TiO}_2$  core/shell nanocubes (0.2 g) were dissolved in 10 mL of hydrochloric acid solution (0.5 M). The mixture was ultrasonicated at room temperature for 10 min; then, the resulting suspension was transferred to a high-pressure reaction vessel and placed at 100 °C for 24 h. The resulting mixture was centrifuged and washed several times with deionized water and absolute ethanol (until the pH approached 7) and finally dried overnight in an oven at 60 °C. The obtained product is labeled as TC-1 with a yield of 52.3%.

**2.3. Hollow Box  $\text{TiO}_2$  Nanocrystals Grown by Homogeneous Nucleation Methods.** **2.3.1. Topological Phase Change Method.** The homogeneous nucleation of  $\text{TiOF}_2$  was prepared according to ref 52. Under magnetic stirring, 15.0 mL of TBOT and 30.0 mL of glacial acetic acid ( $\text{CH}_3\text{COOH}$ ) were poured into a 100 mL beaker. Then, 5.0 mL of hydrofluoric acid was slowly added to the evenly mixed solution. After 10 min of sonication and 30 min of magnetic stirring, both acid mixtures were transferred to a high-pressure reaction vessel and reacted at 200 °C for 12 h. The resulting supernatant was poured off, leaving a grayish-white precipitate.

The precipitate was transferred to a clean plastic bottle containing deionized water, vigorously shaken, and allowed to settle. After complete settling of the precipitate, the supernatant was poured off, and this process was repeated three times. The product was then washed and filtered with anhydrous ethanol. After filtration, the product was dried overnight in a vacuum drying oven at 60 °C and ground in an agate mortar. The obtained white powdered product is  $\text{TiOF}_2$ .

Under ultrasonic conditions, 0.5 g of  $\text{TiOF}_2$  was mixed with 40.0 mL of absolute ethanol in the inner chamber of a reaction vessel. After complete mixing, the mixture was reacted in an oven at 200 °C for 12 h. After the reaction, the precipitate was washed with deionized water and absolute ethanol, suction-filtered, and dried overnight in a vacuum drying oven at 60 °C, resulting in  $\text{TiO}_2$ . Labeled as TC-2, the yield was 95.1%.

**2.3.2. Sonic Solvothermal Method.** 0.50 g of  $\text{TiOF}_2$  was weighed into the inner chamber of a reaction vessel and poured into 40 mL of ethylene glycol. After 10 min of ultrasonic dispersion and 30 min of stirring, the mixture was transferred to a high-pressure reaction vessel and reacted at 220 °C (180, 200, 240 °C) for 8 h. Upon completion of the reaction, the upper clear liquid was decanted; then, the product was washed and suction-filtered with deionized water and absolute ethanol. The product was dried in a vacuum drying oven at 60 °C for 6 h to obtain  $\text{TiO}_2$ , and the sample was labeled as TC-3 with a yield of 97.3%.

**2.3.3. Air Atmosphere Sintering Method.** 0.5 g of  $\text{TiOF}_2$  (0.5 g) was added to a 50.0 mL crucible. The crucible was heated in a muffle furnace at a heating rate of 5 °C/min until it reached 350 °C. The temperature was maintained at 350 °C for 4 h, and then the crucible was cooled back to room

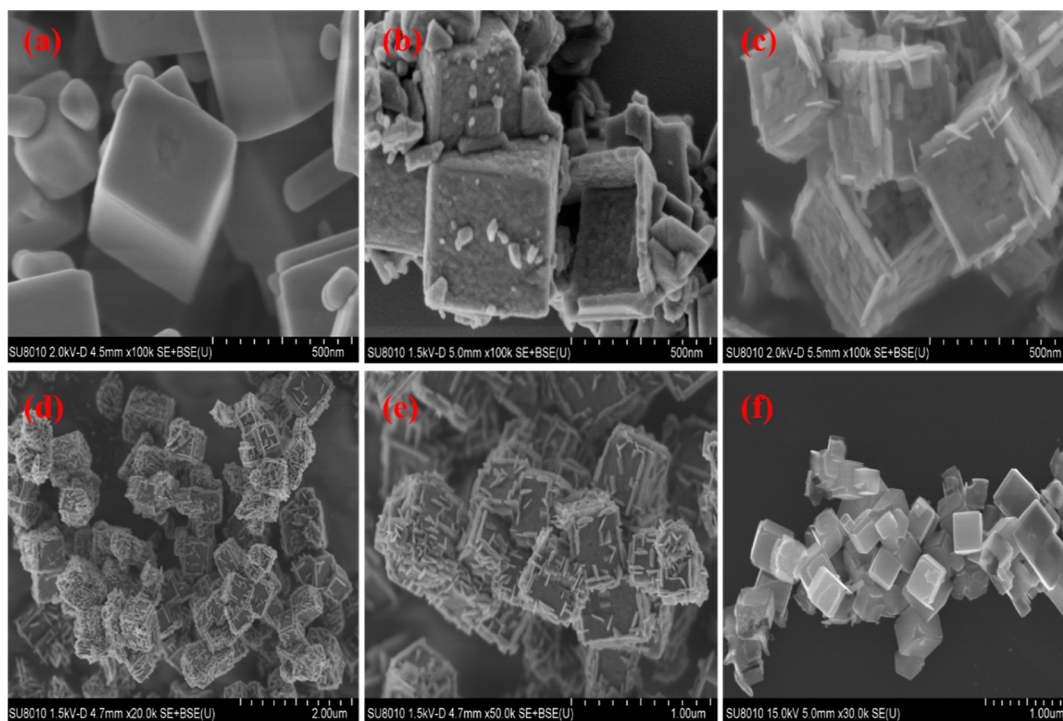


**Figure 2.** SEM characterization of TiO<sub>2</sub> (a), TC-1 (b), TC-2 (c), and TC-3 (d) with a larger enlarged size of TC-3 (e) and TC-4 (f).

temperature at a cooling rate of 5 °C/min to obtain TiO<sub>2</sub>. It was labeled as TC-4, with a yield of 89.2%. The schematic diagram for the growth of hollow box TiO<sub>2</sub> nanocrystals using four methods is shown in Figure 1.

**2.4. Characterization Instruments.** Under an accelerating voltage of 200 kV, the morphology and structure of the samples were examined using a scanning electron microscope (SEM) and transmission electron microscope (TEM) (Tecnaï G 20, USA). X-ray diffraction (XRD) analysis of the samples was conducted using a D8-advance X-ray diffractometer (Bruker, Germany) with Cu K $\alpha$  radiation and a scanning rate of 0.02°/0.1 s. Infrared spectra and X-ray photoelectron spectroscopy (XPS) were, respectively, obtained using a Fourier transform infrared spectrometer (Nexus 470, Shimadzu, Japan) and a Kratos XSAM800 XPS system with Mg K $\alpha$  radiation. The specific surface area and porosity of the samples were determined using a nitrogen adsorption instrument (3 H-2000PS2, Beijing). Ultraviolet–visible diffuse reflectance spectroscopy (UV–vis DRS) and photoluminescence (PL) spectra of the samples were measured by using a UV2600 spectrophotometer (Shimadzu, Japan) and a fluorescence spectrophotometer (F-7000, Hitachi, Japan), respectively. Nitrogen adsorption–desorption isotherms and the BET specific surface area (SBET) of the samples were detected through physical adsorption using a Micromeritics instrument (ASAP 2020, Micromeritics, USA). The photocurrent of the samples was measured using a CHI 660D electrochemical workstation (CH Instruments, Shanghai, China) with nanostructured materials on an FTO working electrode, a saturated Ag/AgCl reference electrode, and a platinum counter electrode. Photocatalytic hydrogen production experiments were conducted using a tandem automatic sampling system (Labsolar 6A, Perfect Light) and a gas chromatograph (GC-9790II, Zhejiang Fulite).

**2.5. Photocatalytic Performance Research.** The photocatalytic hydrogen production experiment was conducted

under simulated solar light by using a xenon lamp. In this experiment, a solution containing 0.04 g of catalyst, 0.025 mol of Na<sub>2</sub>SO<sub>3</sub>, and 0.035 mol of Na<sub>2</sub>S sacrificial agent in 100 mL was added to the reactor. The system was evacuated for 30 min. The solution was continuously stirred, and water circulation cooling was provided in the interlayer of the reactor. During the experiment, every 30 min, the generated gases were automatically collected by using an online gas automatic sampling system. The hydrogen content was analyzed by using gas chromatography.

Catalytic degradation experiments of the model dye molecules RhB and MB were conducted under simulated solar light using a xenon lamp. In a cylindrical Pyrex flask, 50.0 mL of RhB or MB solution ( $1.0 \times 10^{-5}$  mol/L) and 40.0 mg of photocatalyst were poured. After ultrasonic treatment, the solution was stirred in the dark for 30 min to establish the adsorption–desorption equilibrium. Then, the solution was irradiated with a xenon lamp (350 W), and 3.0 mL suspension samples were collected every 10 min. The collected solution was centrifuged to remove the photocatalyst particles. The concentration of RhB and MB in the solution was monitored by UV–vis spectroscopy at 555 nm.

We employed 4-chloro-7-nitrobenzofurazan (NBD-Cl) and coumarin probe molecules along with photopolymerization techniques to detect the active species, hydroxyl radicals ( $\cdot\text{OH}$ ) and superoxide radicals ( $\cdot\text{O}_2^-$ ), of the photocatalyst. A mixture of 0.4 mmol/L NBD-Cl or coumarin with the photocatalyst (1.0 g/L) was prepared, and the suspension was stirred overnight. Subsequently, this suspension was placed under a 210 W xenon lamp. Samples were collected every 2 min and filtered to obtain the filtrate. The fluorescence intensity of the filtrate was measured using a fluorescence spectrophotometer at excitation wavelengths of 454 and 550 nm, respectively.

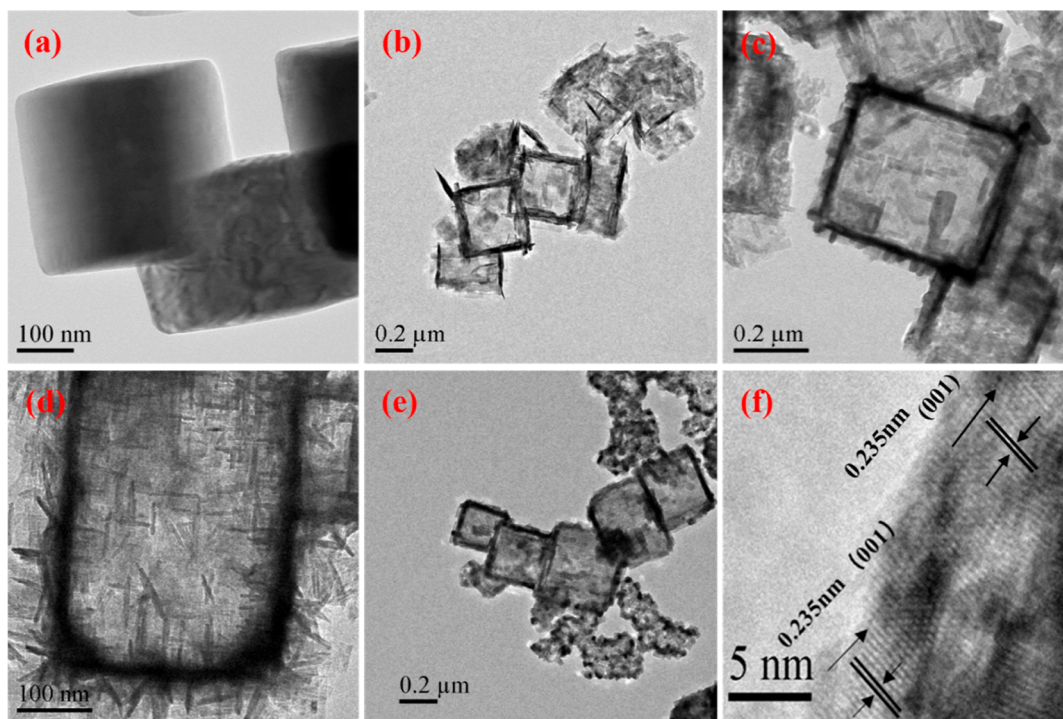


Figure 3. TEM characterization of  $\text{TiOF}_2$  (a), TC-1 (b), TC-2 (c), TC-3 (d), and TC-4 (e) and HR-TEM characterization of TC-3 (f).

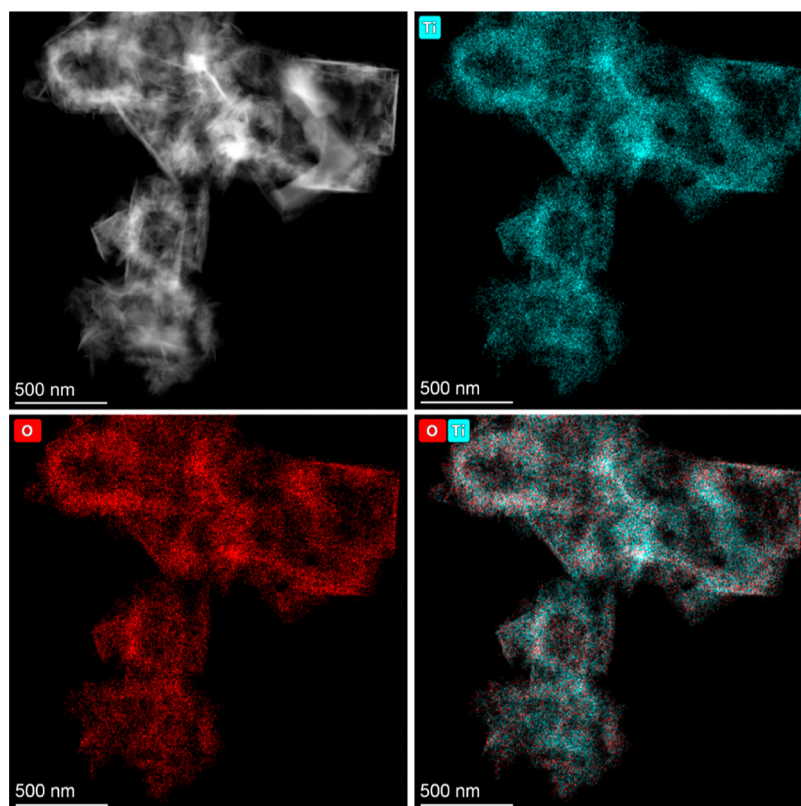
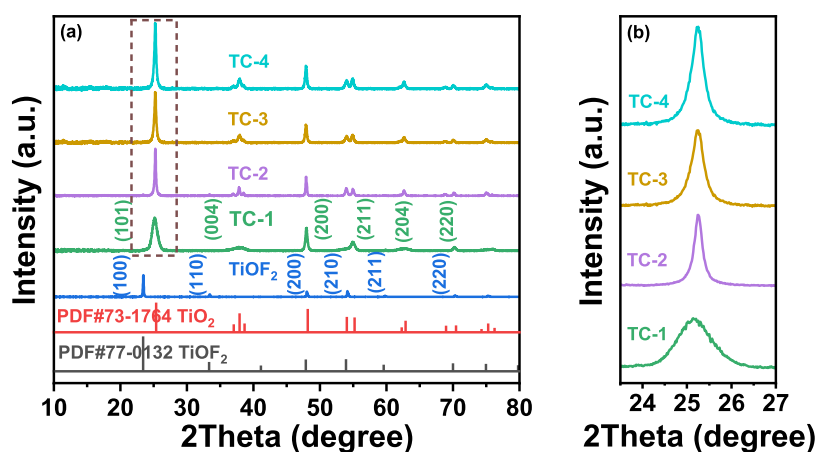


Figure 4. EDS of TC-3.

### 3. RESULTS AND DISCUSSION

**3.1. Morphological Characterization.** The morphological characteristics of  $\text{TiOF}_2$  and hollow box  $\text{TiO}_2$  nanocrystals were observed using a scanning electron microscope (SEM), as depicted in Figure 2. From Figure 2a, it can be observed that

the edge length of the prepared cubic  $\text{TiOF}_2$  crystals was approximately 290 nm. Some of the  $\text{TiOF}_2$  crystals exhibited a nanorod-like shape, while the majority had a cubic crystal structure with a smooth surface. These cubes were solid cubes. The size of  $\text{TiO}_2$  grown by the four methods was approximately 285 nm. Figure 2b illustrates that TC-1 has a



**Figure 5.** X-ray diffraction patterns of the samples (a) and high-resolution diffraction patterns of the samples (b).

distinct, hollow cubic structure. Due to the incomplete dissolution of some  $\text{Fe}_2\text{O}_3$ , the structure of some hollow box  $\text{TiO}_2$  nanocrystals was not entirely intact. Some  $\text{TiO}_2$  shells were unstable and were removed as the core dissolved. As shown in Figure 2c, TC-2 exhibited a box-like shape with a rough surface, and some  $\text{TiO}_2$  nanosheets were attached. These hollow box  $\text{TiO}_2$  nanocrystals had a complete structure composed of six nanofaces. This structure provided a larger contact area for  $\text{TiO}_2$  and dyes. From Figure 2d, TC-3 displayed a three-dimensional multilevel hollow box structure composed of numerous  $\text{TiO}_2$  nanosheets, with many nanosheets embedded on the surface of the hollow nanoboxes. Figure 2e provides a larger-sized image, further demonstrating the multilevel hollow box structure of TC-3. As shown in Figure 2f, TC-4 had six smooth surfaces and exhibited a hollow box structure. However, due to the high reaction temperature in the air atmosphere sintering method, some hollow boxes may become fractured. The surface energy of the system tends to remain at a minimum, leading to structural stacking and a reduction of the surface energy.

Transmission electron microscopy (TEM) was employed to investigate the microstructures of  $\text{TiOF}_2$  crystals and hollow box  $\text{TiO}_2$  nanocrystals. Figure 3a shows that  $\text{TiOF}_2$  exhibited a standard solid cubic crystal structure. From Figure 3b, it can be observed that only some of the TC-1 had a hollow box structure, while others had a solid cubic structure. This suggests that the yield of hollow box  $\text{TiO}_2$  nanocrystals prepared by the acid dissolution denucleation method is low because some  $\text{Fe}_2\text{O}_3$  may not fully dissolve. All TC-2 was primarily a hollow box structure (Figure 3c), indicating a higher yield of hollow box  $\text{TiO}_2$  nanocrystals prepared by the topological phase transformation method. Figure 3d displays the three-dimensional multilevel hollow box structure of TC-3, with various sizes of linear structures (nanosheets) surrounding the boxes. Figure 3e clearly shows that TC-4 had a hollow box-like structure with a noticeable stacking arrangement. High temperatures can prevent some  $\text{TiO}_2$  from forming a hollow box structure, leading to a lower yield of hollow box  $\text{TiO}_2$  nanocrystals prepared by the air atmosphere sintering method. These TEM results are consistent with the SEM morphological characterizations. Figure 3f is an HR-TEM image of TC-3, with a lattice spacing of 0.235 nm corresponding to the (001) facet of anatase  $\text{TiO}_2$ , indicating that the exposed surface of TC-3 is mainly the (001) facet.

Figure 4 shows the energy-dispersive spectroscopy (EDS) of TC-3. From the figure, it can be observed that TC-3 contained two elements, O and Ti. The O elements (red) and Ti elements (cyan) were distributed on the surface of the hollow box and the nanosheets on the surface, further confirming the multilevel hollow box structure of TC-3.

**3.2. XRD, FT-IR, and Raman Characterization.** Figure 5a shows the X-ray diffraction patterns (XRD) of the samples. The diffraction peaks of  $\text{TiOF}_2$  matched the standard card (PDF#77-0132), with  $2\theta$  values of 23.45, 33.46, 48.04, and 54.14° corresponding to the (100), (110), (200), and (210) crystal facets of  $\text{TiOF}_2$ , respectively. By comparison of the XRD pattern of the  $\text{TiO}_2$  samples with that of  $\text{TiOF}_2$ , no characteristic diffraction peak of  $\text{TiOF}_2$  was observed in  $\text{TiO}_2$ , indicating the complete conversion of  $\text{TiOF}_2$  to  $\text{TiO}_2$ . This is consistent with the conclusions drawn from SEM and TEM. When compared to the standard card (PDF#73-1764),  $\text{TiO}_2$  prepared by the four methods is in the standard anatase phase, with  $2\theta$  values of 25.21, 37.83, 47.95, 54.94, and 62.62° corresponding to the (101), (004), (200), (211), and (204) crystal facets of anatase  $\text{TiO}_2$ . This is attributed to the role of F as structure-directing agents.<sup>53</sup> The high-resolution diffraction pattern of the  $\text{TiO}_2$  (101) facet is shown in Figure 5b. It can be observed that the diffraction peaks of TC-1 to TC-4 become sharper, indicating that the crystallinity of the prepared  $\text{TiO}_2$  increases.<sup>54</sup>

As shown in Table 1, the crystal size of  $\text{TiO}_2$  was determined based on the (101) diffraction peak using the Scherrer equation:  $D = K\lambda/\beta \cos \theta$ , where  $\lambda$  and  $\theta$  represent the X-ray wavelength and X-ray diffraction angle, respectively. In the calculations, the full width at half-maximum ( $\beta$ ) of the

**Table 1.** Crystal Size and Crystal Lattice Parameters of  $\text{TiO}_2$

samples	XRD <sub>(101)</sub> peak (deg)	XRD <sub>(101)</sub> relative intensity (%)	crystal size <sup>a†</sup> (nm)	crystal lattice parameters		
				a/nm	b/nm	c/nm
TC-1	25.14	31	282	0.3787	0.3787	0.9682
TC-2	25.25	36	282	0.3794	0.3794	0.9503
TC-3	25.25	33	288	0.3797	0.3797	0.9418
TC-4	25.25	38	285	0.3791	0.3791	0.9344

<sup>a†</sup>Determined by the Scherrer equation based on the diffraction peak of the (101) facet.

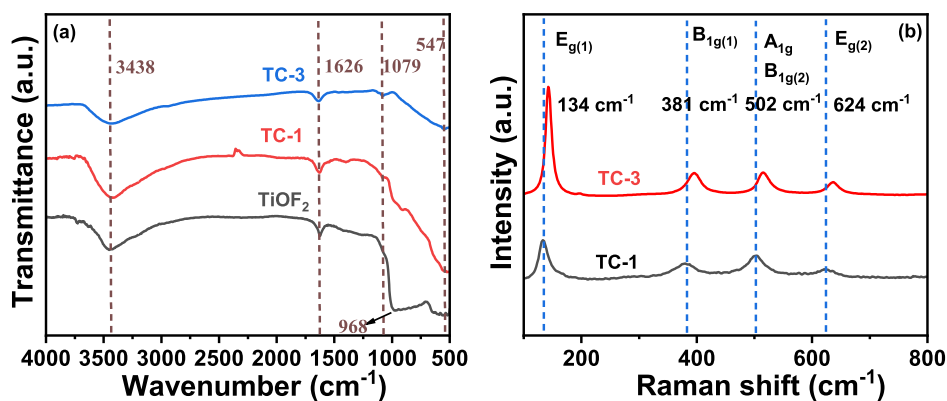


Figure 6. FT-IR characterization of  $\text{TiOF}_2$ , TC-1, and TC-3 (a). The Raman spectra of TC-1 and TC-3 (b).

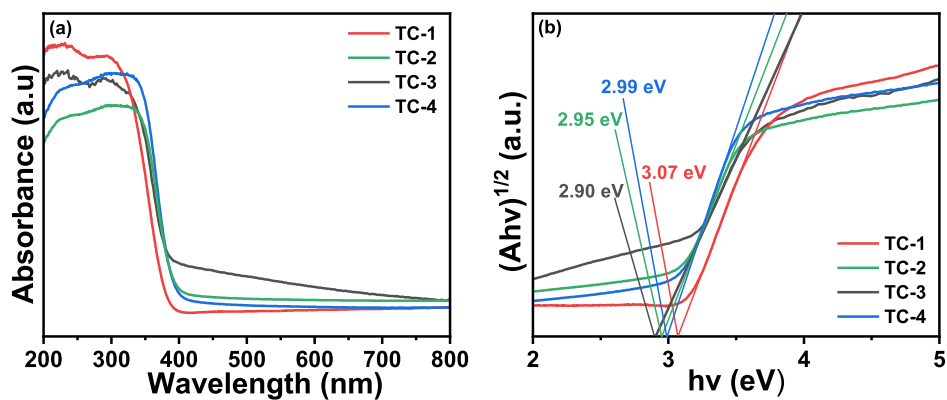


Figure 7. UV-vis diffuse reflectance spectra of the samples (a) and the curve of  $(ah\nu)^2$  versus  $h\nu$  for the samples (b).

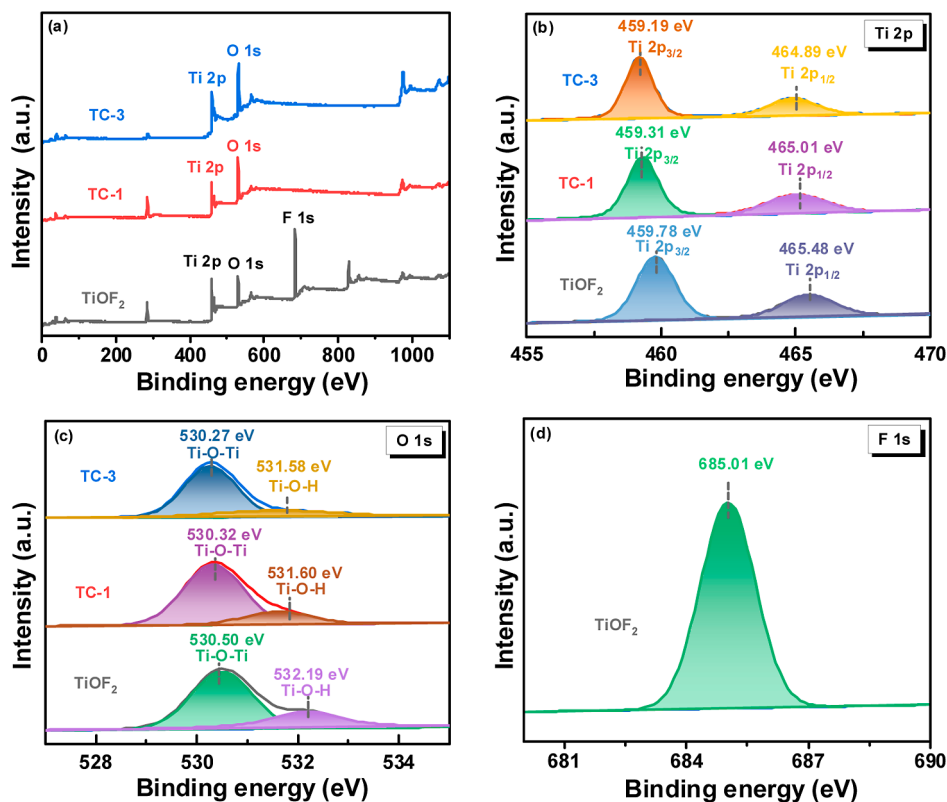


Figure 8. XPS spectra of full spectra (a), Ti 2p (b), O 1s (c), and F 1s (d).

diffraction peak was chosen, and the shape factor ( $K$ ) was determined to be 0.89. From the calculated results, it can be observed that the crystal sizes of  $\text{TiO}_2$  prepared by the four methods are quite similar. The lattice parameters of  $\text{TiO}_2$  were calculated using Bragg's law ( $2d \sin \theta = \lambda$ ) and the formula ( $(1/d^2) = (h^2 + k^2/a^2) + (l^2/c^2)$ ). The lattice constants of  $\text{TiO}_2$  prepared by the four methods also show little variation, indicating excellent control over the size of  $\text{TiO}_2$ .

Figure 6a shows the FT-IR spectra for  $\text{TiOF}_2$ , TC-1, and TC-3. The peak at  $3438 \text{ cm}^{-1}$  corresponds to the stretching vibration of the surface  $-\text{OH}$  groups and adsorbed water on the sample. At  $1626 \text{ cm}^{-1}$ , there is an absorption peak associated with the stretching and bending vibrations of surface water. The characteristic absorption peak at  $1079 \text{ cm}^{-1}$  is attributed to the  $\text{Ti}-\text{O}-\text{Ti}$  bonds in  $\text{TiO}_2$ .<sup>55</sup> The absorption peak at a central wavenumber of  $968 \text{ cm}^{-1}$  is assigned to the stretching vibration of  $\text{Ti}-\text{F}$  bonds in  $\text{TiOF}_2$ . The stretching vibrational absorption peak of  $\text{Ti}-\text{O}$  in the sample is around  $547 \text{ cm}^{-1}$ . All of the characteristic peaks of both  $\text{TiOF}_2$  and  $\text{TiO}_2$  are included in the graph, indicating the successful preparation of  $\text{TiOF}_2$  and  $\text{TiO}_2$ . In order to further investigate the structure of  $\text{TiO}_2$ , Raman spectroscopy was conducted on  $\text{TiO}_2$ . Figure 6b shows the characteristic Raman spectra of TC-1 and TC-3. Peaks centered at 134, 381, 502, and  $624 \text{ cm}^{-1}$  correspond to the  $E_g^{(1)}$ ,  $B_{1g}^{(1)}$ ,  $A_{1g}^{(1)}/B_{1g}^{(2)}$ , and  $E_g^{(2)}$  Raman modes of anatase  $\text{TiO}_2$ , respectively.<sup>56</sup> These characteristic spectra are located in the low-frequency region ( $100\text{--}800 \text{ cm}^{-1}$  Raman shifts) of the prepared  $\text{TiO}_2$ , further confirming them as anatase  $\text{TiO}_2$ , consistent with XRD results. In comparison to TC-1, the peak positions in TC-3 had shifted by approximately  $10 \text{ cm}^{-1}$ , which may be related to differences in the concentration of structure-directing agent F. At the same time, the intensity of the peaks has significantly increased, indicating the crystalline enhancement of  $\text{TiO}_2$ .

**3.3. UV-Visible DRS Characterization.** Figure 7a shows the UV-visible diffuse reflectance spectra (DRS) of the samples. From the graph, it can be observed that TC-1 exhibits minimal absorption in the visible light range ( $400\text{--}800 \text{ nm}$ ) but significant absorption in the ultraviolet region ( $200\text{--}400 \text{ nm}$ ). However, TC-2 and TC-4 showed some absorption in the visible-light region. This suggests that the hollow structure itself enhances visible light absorption to some extent. Compared to  $\text{TiO}_2$  prepared by other methods, TC-3 exhibited a more substantial absorption in the visible light region. This is likely due to the multilayered hollow box structure of TC-3, which increased the number of active reaction sites, thereby expanding the range of responses to visible light and improving photocatalytic performance. Figure 7b shows the Kubelka-Munk transformed reflectance spectra of the samples. Bandgap values were calculated using the tangent method, which is the point where the tangent to the curve intersects the  $x$ -axis.<sup>57</sup> The bandgap values for TC-1, TC-2, TC-3, and TC-4 are 3.07, 2.95, 2.90, and 2.99 eV, respectively. The results indicated that TC-3 with the multilayered hollow box structure has the narrowest bandgap.

**3.4. XPS Characterization.** Figure 8a displays the surface composition of  $\text{TiOF}_2$  and  $\text{TiO}_2$  as revealed by X-ray photoelectron spectroscopy (XPS). The  $\text{TiOF}_2$  sample contained C, Ti, O, and F elements, while the  $\text{TiO}_2$  samples contained C, Ti, and O elements, with the presence of C likely originating from the measurement instrument. Figure 8b-d shows high-resolution XPS images for Ti 2p, O 1s, and F 1s, respectively. From Figure 8b, it can be observed that the Ti

$2p_{3/2}$  and Ti  $2p_{1/2}$  peaks of  $\text{TiOF}_2$  appear at 459.78 and 465.48 eV, respectively. For TC-1, the Ti  $2p_{3/2}$  and Ti  $2p_{1/2}$  peaks are at 459.31 and 465.01 eV, while for TC-3, they are at 459.19 and 464.89 eV, respectively. The difference between the two peaks is 5.7 eV in all cases, indicating that Ti in both  $\text{TiOF}_2$  and  $\text{TiO}_2$  is in the +4 state. From Figure 8c, the  $\text{Ti}-\text{O}-\text{Ti}$  peaks for  $\text{TiOF}_2$ , TC-1, and TC-3 occur at 530.50, 530.32, and 530.27 eV, respectively. Additionally, the  $\text{Ti}-\text{O}-\text{H}$  peaks for  $\text{TiOF}_2$ , TC-1, and TC-3 appear at 532.19, 531.60, and 531.58 eV, respectively. Compared to TC-1, TC-3 showed a negative shift in both Ti 2p and O 1s peaks, suggesting a higher electron cloud density around TC-3. Figure 8d reveals that the F 1s peak for  $\text{TiOF}_2$  appears at 685.01 eV. These results confirm the successful preparation of  $\text{TiOF}_2$  and  $\text{TiO}_2$ .

**3.5. Comparison of Growth Conditions for Hollow Box  $\text{TiO}_2$  Nanocrystals by the Acid Dissolution Denucleation Method, the Topological Phase Transition Method, the Sonic Solvothermal Method, and the Air Atmosphere Sintering Method.** The reaction conditions for the four methods are compared, as shown in Table 2. The acid dissolution denucleation method for growing

**Table 2. Comparison of Conditions for the Growth of Hollow Box  $\text{TiO}_2$  Nanocrystals by Four Methods**

methods	acid dissolution denucleation method (TC-1)	topological phase transition method (TC-2)	sonic solvothermal method (TC-3)	air atmosphere sintering method (TC-4)
nuclei	$\text{Fe}_2\text{O}_3$	$\text{TiOF}_2$	$\text{TiOF}_2$	$\text{TiOF}_2$
temperature	$60^\circ\text{C}$	$200^\circ\text{C}$	$220^\circ\text{C}$	$350^\circ\text{C}$
reaction time	24 h	12 h	8 h	4 h
yield	about 52.3%	about 95.1%	about 97.3%	about 89.2%

hollow box  $\text{TiO}_2$  nanocrystals is time-consuming with mild reaction conditions.  $\text{TiO}_2$  was obtained after 24 h of reaction at  $45^\circ\text{C}$ , with a yield of only 52.3%. The topological phase transition method takes more time and has a lower reaction temperature. The reaction is carried out at  $200^\circ\text{C}$  with a yield of approximately 95.1%. The sonic solvothermal method also takes some time and has a higher reaction temperature of  $220^\circ\text{C}$ . The yield is as high as 97.3%. The air atmosphere sintering method has a short reaction time but a high temperature, and the conditions are demanding. The reaction temperature is  $350^\circ\text{C}$ , with a yield of about 89.2%.

**3.6. Growth Mechanism of  $\text{TiOF}_2$  and Hollow Box  $\text{TiO}_2$  Nanocrystals.** **3.6.1. Growth Mechanism of  $\text{TiOF}_2$ .**  $\text{TiOF}_2$  was grown using a solvothermal method with TBOT as the titanium source and HF as the fluorine source and exhibited a regular shape, high purity, and good crystallinity. The possible growth mechanism is depicted in Figure 9. TBOT undergoes a transesterification reaction with acetic acid, where one of TBOT's butoxy groups is replaced by an acetate group. It then reacts with HF, forming TBOT substituted with one F atom. After a repeat of this cycle, TBOT substituted with two F atoms is obtained. It reacts with acetic acid in an esterification reaction to form  $\text{Ti}(\text{OH})_2\text{F}_2$ , which finally undergoes a dehydration condensation to produce  $\text{TiOF}_2$ .

**3.6.2. Growth Mechanism of Hollow Box  $\text{TiO}_2$  Nanocrystals by the Acid Dissolution Denucleation Method.** First,  $\text{Fe}_2\text{O}_3/\text{TiO}_2$  core/shell nanocubes were grown by using a kinetic control encapsulation method. Then, hollow box  $\text{TiO}_2$  nanocrystals were grown by weak acid corrosion of the

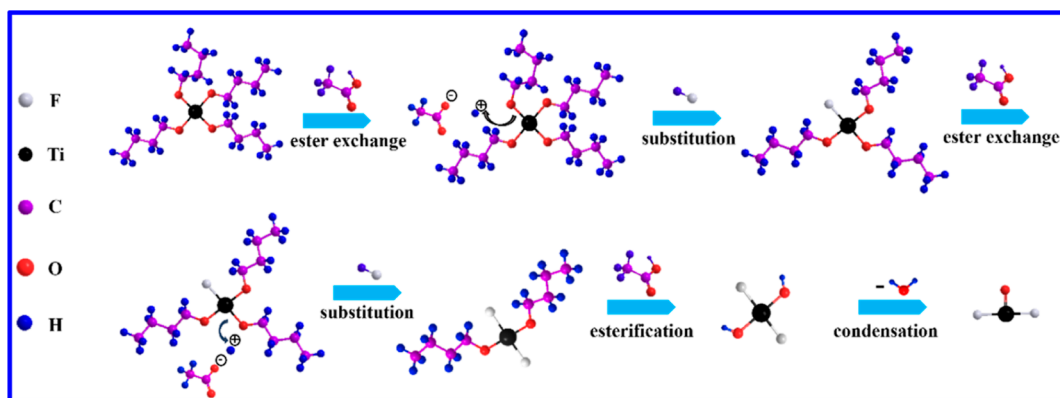


Figure 9. Growth mechanism of precursor  $\text{TiOF}_2$  by tetrabutyl titanate.

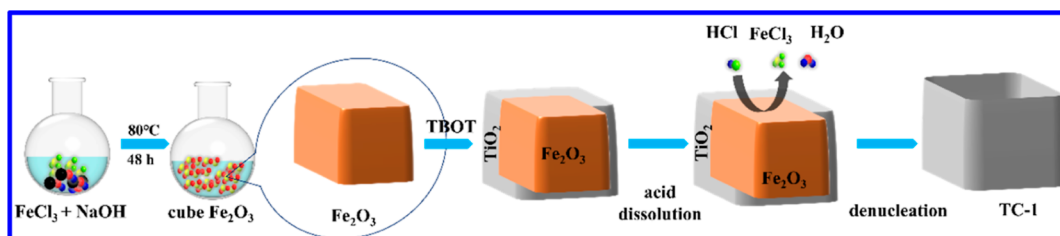


Figure 10. Growth mechanism of hollow box  $\text{TiO}_2$  nanocrystals by the acid dissolution denucleation method.

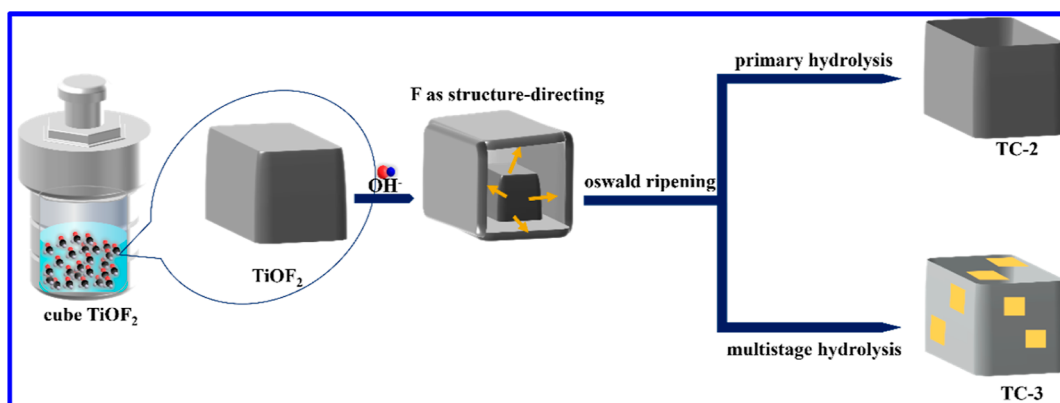
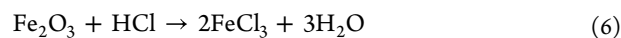
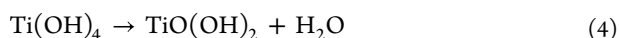
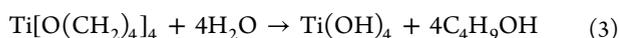
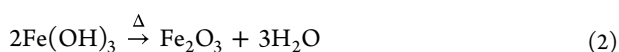
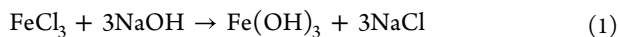


Figure 11. Growth mechanism of hollow box  $\text{TiO}_2$  nanocrystals by the topological phase change method or the sonic solvothermal method.

hematite ( $\text{Fe}_2\text{O}_3$ ) core. The reaction equations are shown in eqs 1–6, and the mechanism is shown in Figure 10. Under ethanol alkaline conditions, titanium tetrabutoxide was hydrolyzed and aged on the surface of the  $\text{Fe}_2\text{O}_3$  nanocubes, forming  $\text{Fe}_2\text{O}_3/\text{TiO}_2$  core/shell nanocubes. Hydrochloric acid (HCl) entered the pores of  $\text{TiO}_2$  and reacted with  $\text{Fe}_2\text{O}_3$ , resulting in the formation of an  $\text{FeCl}_3$  solution. This  $\text{FeCl}_3$  solution flowed out of the pores, resulting in the formation of hollow box  $\text{TiO}_2$  nanocrystals.



**3.6.3. Growth Mechanism of Hollow Box  $\text{TiO}_2$  Nanocrystals by the Topological Phase Transition Method or the Sonic Solvothermal Method.** The principle behind the growth of hollow box  $\text{TiO}_2$  nanocrystals using the topological phase transition method or the sonic solvothermal method is Oswald ripening. This means that relatively smaller solute particles and crystals within the solution dissolve first and then accumulate on the surfaces of relatively larger solute particles and crystals.<sup>58</sup> This theory is derived through reverse deduction, meaning that the molecular energy on the surface of particles is higher than the molecular energy inside the particles, thus making them unstable. The reaction equations are shown in eqs 7–13, and the mechanism is shown in Figure 11. The surface of  $\text{TiOF}_2$  undergoes hydrolysis with hydroxide ions in solution, resulting in the formation of titanium hydroxide. Titanium hydroxide then dehydrates to form  $\text{TiO}_2$ , creating larger crystal facets on the surface of the original crystal.  $\text{TiOF}_2$  cubic crystals exhibit a porous structure, and  $\text{OH}^-$  ions attack

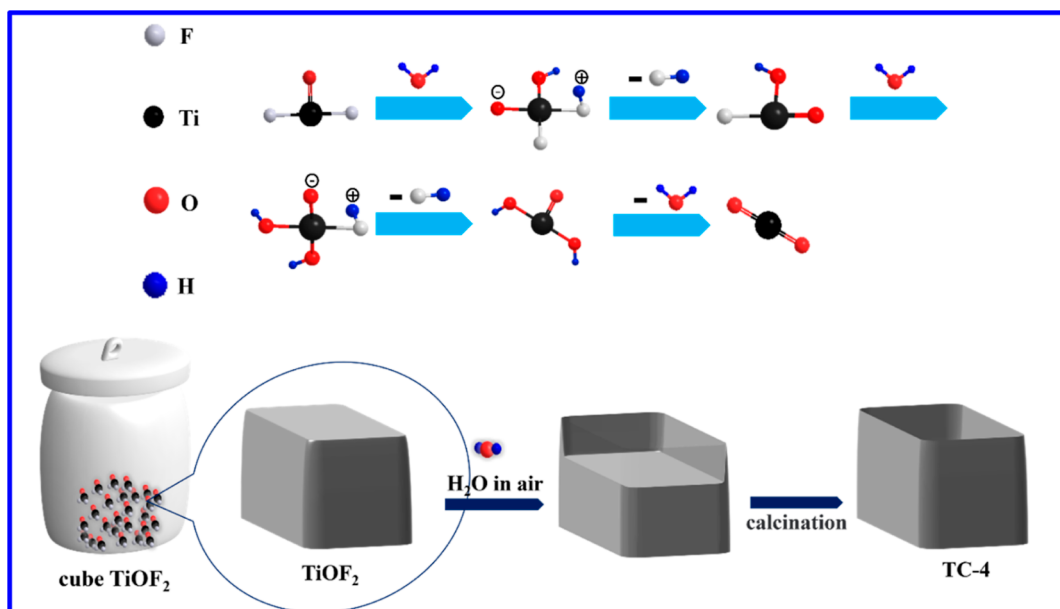


Figure 12. Growth mechanism of hollow box  $\text{TiO}_2$  nanocrystals by the air atmosphere sintering method.

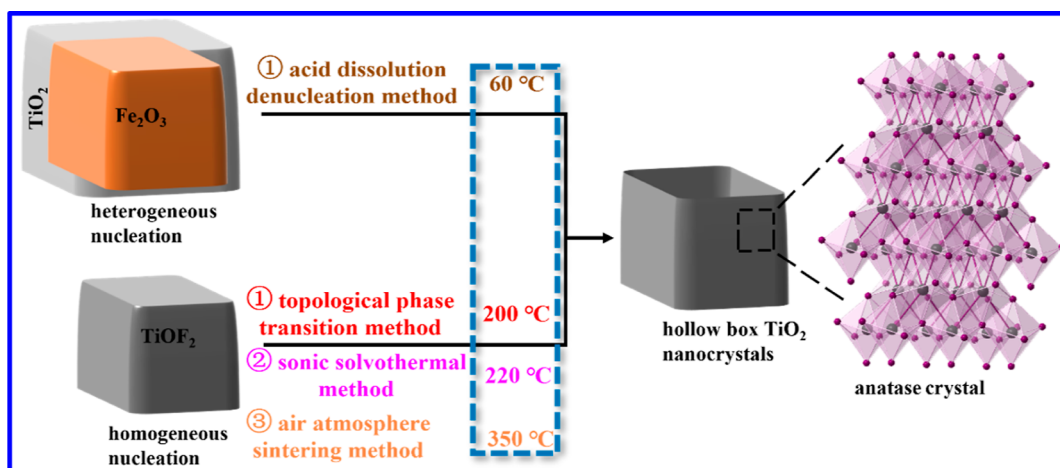
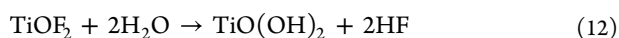
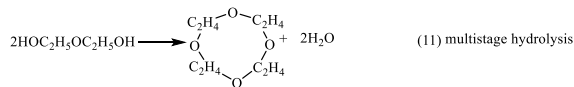
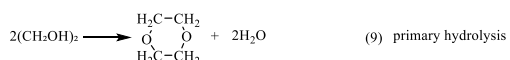


Figure 13. Hollow box  $\text{TiO}_2$  nanocrystals grown by four nucleation methods.

$\text{TiOF}_2$  from various directions, forming  $\text{TiO}(\text{OH})_2$  on both the internal and external surfaces. Dissolution of  $\text{TiO}_2$  particles generated by dehydration, which then deposit onto the nanoscale surface composed of  $\text{TiO}_2$ . These six surfaces come together to form hollow box  $\text{TiO}_2$  nanocrystals.



**3.6.4. Growth Mechanism of Hollow Box  $\text{TiO}_2$  Nanocrystals by the Air Atmosphere Sintering Method.** As shown in Figure 12, the growth of hollow box  $\text{TiO}_2$  nanocrystals using the air atmosphere sintering method involves a hydrolysis reaction.  $\text{TiOF}_2$  reacts with water vapor in air within a muffle furnace. Specifically, the cubic surface of  $\text{TiOF}_2$  starts to undergo hydrolysis, resulting in the formation of tiny  $\text{TiO}_2$  nanosheets. The reaction primarily involves two steps.  $\text{TiOF}_2$  reacts with water vapor, losing a molecule of HF, resulting in the substitution of one F on  $\text{TiOF}_2$  with a hydroxyl group. Then, after this cycle is repeated once,  $\text{TiO}(\text{OH})_2$  is formed. This compound loses a molecule of  $\text{H}_2\text{O}$  to form  $\text{TiO}_2$ . Further hydrolysis of the  $\text{TiOF}_2$  cube results in the formation of hollow box  $\text{TiO}_2$  nanocrystals composed of six nanosheets.

The morphologies of 3D hollow box  $\text{TiO}_2$  nanocrystals grown using the four methods are slightly different but all are composed of anatase-phase nanocrystals. Figure 13 is a schematic representation of the synthesis of hollow box  $\text{TiO}_2$  nanocrystals using these four methods.

**3.7. Evolution Process of Hollow Box  $\text{TiO}_2$  Nanocrystals (001) Facets and Calculation of the (001) Facet**

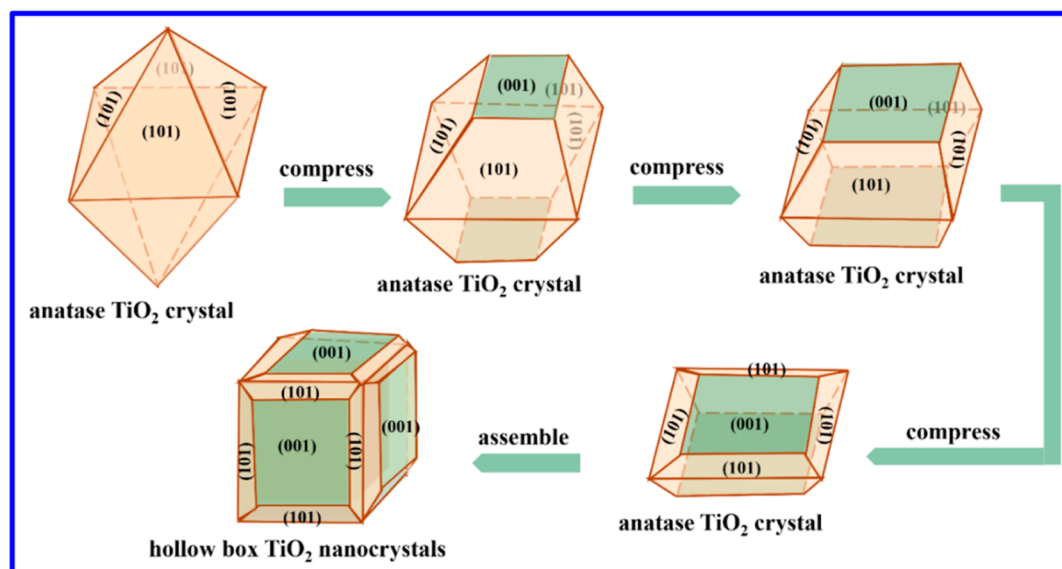


Figure 14. Evolution process of hollow box TiO<sub>2</sub> nanocrystal crystal facets.

**Exposure Ratio.** The formation process of anatase TiO<sub>2</sub> nanocrystals is depicted in Figure 14. Octahedral anatase TiO<sub>2</sub> single crystals gradually undergo compression, leading to the emergence of (001) facets with the area progressively increasing. The lateral area of the octahedron decreases, transforming the anatase TiO<sub>2</sub> single crystal into extremely thin octahedral nanosheets. Six such anatase TiO<sub>2</sub> nanosheets come together to form hollow box TiO<sub>2</sub> nanocrystals.

The formula for calculating the (001) facet exposure rate is as follow<sup>59</sup>

$$\begin{aligned}
 S_{001} \% &= S_{001} / (S_{001} + S_{101}) \\
 &= \frac{2a^2}{2a^2 + 8\left(\frac{1}{2} \times \frac{\frac{1}{2}b}{\cos \theta} \times b - \frac{1}{2} \times \frac{\frac{1}{2}a}{\cos \theta} \times a\right)} \\
 &= \frac{a^2}{a^2 + \frac{b^2 - a^2}{\cos \theta}} = \frac{1}{1 + \frac{b^2 - a^2}{a^2 \cos \theta}} \\
 &= \frac{\cos \theta}{\cos \theta + \frac{b^2}{a^2} - 1} = \frac{\cos \theta}{\cos \theta + \left(\frac{a}{b}\right)^{-2} - 1}
 \end{aligned}$$

In the formula,  $\theta$  is the theoretical value of the surface angle of (001) and (101) crystal facets, and  $b$  and  $a$  are the side length of the bipyramid and the side length of the square at the top of the apical octahedron, respectively, and  $0 \leq a/b \leq 1$ . The (001) facets exposure ratio of hollow box TiO<sub>2</sub> nanocrystals refers to the research of Huang et al.<sup>60</sup> The result is shown in Table 3 below. The (001) facet exposure ratio of TC-3 is the largest. The (001) facet exposure ratio of TC-1 is the smallest. Their (001) facet exposure rates are

Table 3. (001) Crystal Facet Exposure Ratios of the Samples

samples	$\theta$ (deg)	$a$ (nm)	$b$ (nm)	(001) facets exposure ratio (%)
TC-1	63.76	267.6	282	80
TC-2	55.60	270.8	282	87
TC-3	46.16	279.7	288	92
TC-4	58.79	272.8	285	85

different, indicating that the amount of water in reaction conditions affects the (001) facet exposure rate of hollow box TiO<sub>2</sub> nanocrystals. The more water there is, the lower the (001) facet exposure rate of hollow box TiO<sub>2</sub> nanocrystals.

### 3.8. Nitrogen Adsorption and Photovoltaic Research.

In order to obtain more detailed structural information about the prepared hollow box TiO<sub>2</sub> nanocrystals, nitrogen adsorption was used to measure the Brunauer–Emmett–Teller (BET) surface area and pore structure of the hollow box TiO<sub>2</sub> nanocrystals. Figure 15a shows the nitrogen adsorption–desorption isotherms and the corresponding pore size distribution curves for TC-1 and TC-3. Both TC-1 and TC-3 exhibited the shape of the H3 hysteresis loop and type IV isotherm, indicating a slit-like pore shape consistent with the hollow nanobox shape formed by the assembly of six nanosheets of TiO<sub>2</sub>. Table 4 lists the pore volume, average pore size, and BET specific surface area of TC-1 and TC-3. The results indicated that TC-3 had the largest pore volume (0.099 cm<sup>3</sup> g<sup>-1</sup>), average pore size (23.1 nm), and BET specific surface area (17.1 m<sup>2</sup> g<sup>-1</sup>). This may be related to the multilevel hollow box structure of TC-3. Furthermore, a larger specific surface area can provide more active sites to participate in photocatalytic reactions, thus contributing to the improvement of adsorption and photocatalytic performance. Figure 15b shows the photoluminescence spectrum for TC-1 and TC-3. TiO<sub>2</sub> exhibited a pronounced emission peak near 400 nm. Generally, a stronger emission spectrum indicates a higher rate of e<sup>-</sup>–h<sup>+</sup> pair recombination. Compared with TC-1, TC-3 had a weaker photoluminescence (PL) intensity, suggesting a lower rate of e<sup>-</sup>–h<sup>+</sup> pair recombination. This may be attributed to the multilevel structure of TC-3. As shown in Figure 15c, TC-3 exhibited a transient photocurrent response higher than that of TC-1, indicating a higher efficiency of separating photo-generated e<sup>-</sup>–h<sup>+</sup> pairs. The Nyquist plots (EIS) for TC-1 and TC-3 are shown in Figure 15d. Equivalent circuit simulations were performed by using Zview software. CPE1 and CPE2 are constant phase angle elements, R1 and R3 are electrolyte resistances, and R2 is the charge transfer resistance.<sup>61</sup> Compared to TC-1, TC-3 had a smaller radius, indicating a lower electron transfer resistance in TC-3. The results

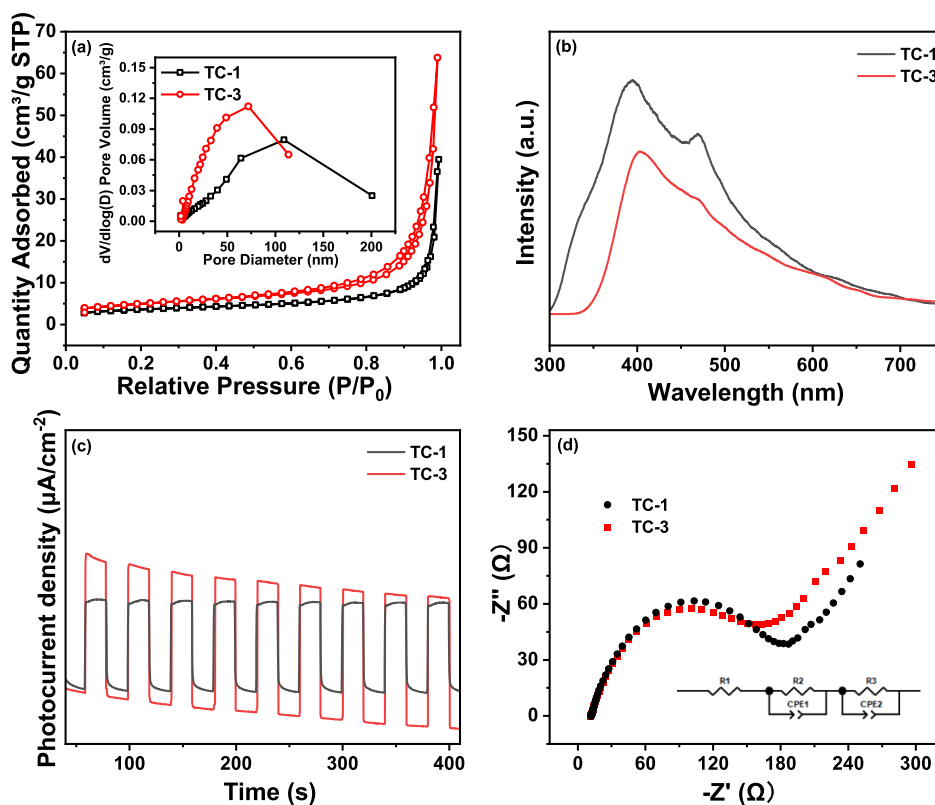


**Figure 15.** Nitrogen adsorption isotherms and corresponding pore size distribution curves of TC-1 and TC-3 (a). PL spectra of TC-1 and TC-3 (b). Photocurrent response diagram of TC-1 and TC-3 (c). EIS of TC-1 and TC-3 (d).

**Table 4. Volume, Mean Pore Size, and Specific Surface Area for TC-1 and TC-3**

samples	$V$ (cm <sup>3</sup> g <sup>-1</sup> )	pore size (nm)	$S_{\text{BET}}$ (m <sup>2</sup> g <sup>-1</sup> )
TC-1	0.054	18.1	12.0
TC-2	0.086	21.4	15.9
TC-3	0.099	23.1	17.1
TC-4	0.067	20.5	14.7

indicated that TC-3 had a faster electron transfer rate and a lower  $e^-$ - $h^+$  pair recombination rate.

**3.9. Photocatalytic Properties of Hollow Box TiO<sub>2</sub> Nanocrystals.** The hydrogen production performance of test samples was evaluated through photocatalytic experiments under simulated sunlight. As shown in Figure 16a, the hydrogen production amounts for TC-1, TC-2, TC-3, and

TC-4 within 4 h are 10.00, 12.97, 15.02, and 11.07 μmol, respectively. TC-3 had the highest hydrogen production, which can be attributed to the multi-hollow box structure of TC-3. From Figure 16b, it can be observed that the hydrogen production rates for TC-1, TC-2, TC-3, and TC-4 are 62.49, 81.08, 93.88, and 69.19 μmol g<sup>-1</sup> h<sup>-1</sup>, respectively. The results indicated that the high (001) facet exposure rate and unique hollow box structure of TiO<sub>2</sub> contribute to enhancing the photocatalytic hydrogen production performance.

By conducting photocatalytic degradation of RhB and MB dyes under Xe lamp irradiation, we explored the differences in photocatalytic activity of hollow box TiO<sub>2</sub> nanocrystals prepared by four methods. Figure 17a shows the change in the  $C/C_0$  ratio of the samples over time  $t$ , where  $C_0$  is the initial concentration of RhB in the aqueous solution, and  $C$  is the remaining concentration of RhB in the solution after

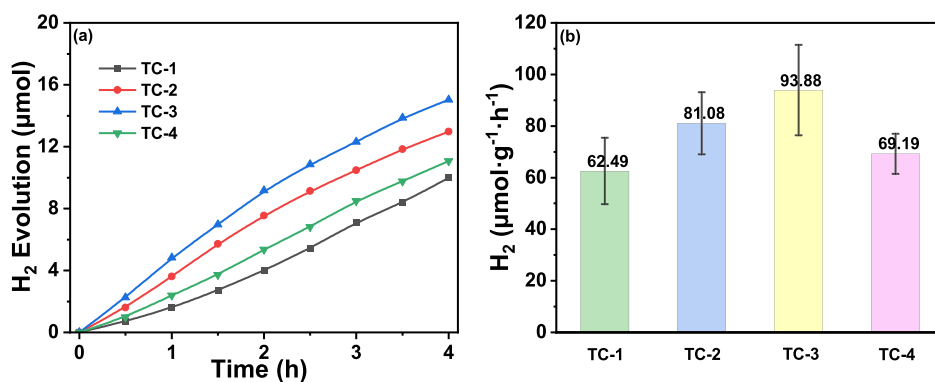


**Figure 16.** Photocatalytic hydrogen production amount over time for the samples (a) and the hydrogen production rate graph of the samples (b).

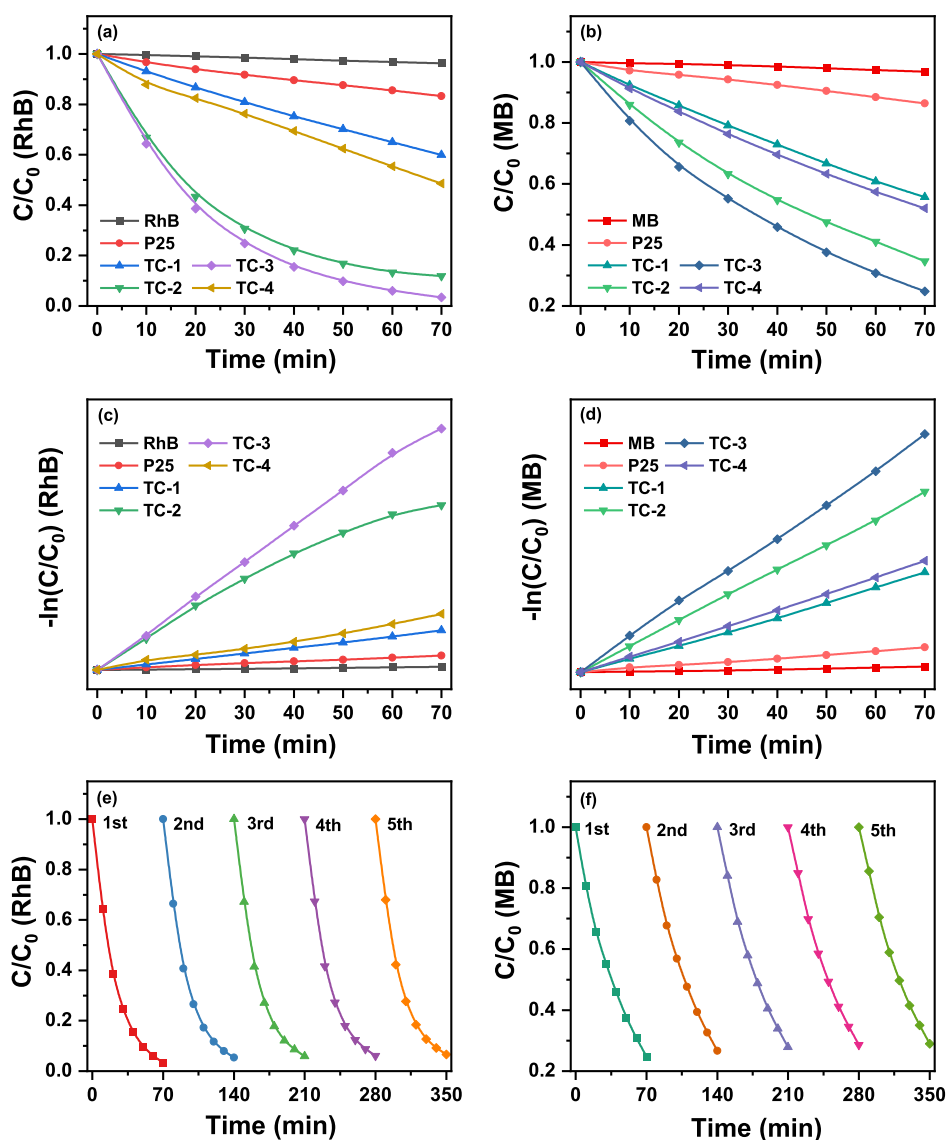


**Figure 17.** RhB photocatalytic degradation plots of the samples (a,b). Plot of  $\ln(C_0/C)$  vs time for the samples (c,d). Cyclic degradation of RhB and MB over the samples (e,f).

degradation. RhB without a catalyst and RhB with were P25 hardly degraded. TC-3 exhibited the best catalytic activity, degrading 96.59% of RhB within 70 min. This is because TC-3 has a larger (001) facet exposure and a multilevel hollow box structure. TC-1 and TC-4 showed relatively poor degradation performance due to their relatively minimal (001) facet exposure and incomplete hollow box structure. Figure 17b represents the degradation rate of the samples with respect to MB, and the reaction follows the Langmuir–Hinshelwood first-order reaction kinetics. The photocatalytic degradation rate constant ( $k$ ) for RhB can be calculated by using the formula  $k = -1/t \ln(C/C_0)$ , where  $C_0$  and  $C$  ( $\text{mg/L}^{-1}$ ) are the concentrations of RhB at time 0 and  $t$  ( $\text{min}^{-1}$ ), respectively. The degradation rate constants for TC-1, TC-2, TC-3, and TC-4 were 0.00725, 0.03111, 0.04556, and 0.00987, respectively. Figure 17c shows the degradation of the samples with respect to MB. The degradation efficiency of the samples toward MB was weaker than that for RhB. The results for the degradation of MB by hollow box  $\text{TiO}_2$  nanocrystals prepared by the four methods were consistent with those for RhB. TC-3 exhibited the best degradation performance, degrading 75.25%

of MB within 70 min. From Figure 17d, the degradation rate constants for TC-1, TC-2, TC-3, and TC-4 were 0.00837, 0.01496, 0.01959, and 0.00932, respectively. Figure 17e,f represents the five-cycle degradation of RhB and MB by TC-3. The results indicate that TC-3 possesses good photocatalytic stability. After five cycles, the degradation rates only decreased by 2.93 and 4.24%.

**3.10. Detection and Capture of Active Species.** Figure 18a,b depicts the detection of active species hydroxyl radicals ( $\cdot\text{OH}$ ) and superoxide radicals ( $\cdot\text{O}_2^-$ ) respectively. With increasing irradiation time, the peak intensities at 454 and 550 nm continuously increase. The results indicate that TC-3 can generate  $\cdot\text{OH}$  and  $\cdot\text{O}_2^-$  under light conditions, and their concentrations increase as time goes on. The capture of active species on TC-3 is shown in Figure 18c. The external conditions for active species capture experiments are consistent with the conditions for RhB photocatalytic degradation. In addition, 0.05 mmol of ethylenediaminetetraacetic acid (EDTA), isopropanol (IPA), benzoquinone (BZQ), and  $\text{AgNO}_3$  were added. EDTA is used to capture  $\text{h}^+$ , IPA captures  $\cdot\text{OH}$ , BZQ captures  $\cdot\text{O}_2^-$ , and  $\text{AgNO}_3$  captures  $\text{e}^-$ . Compared

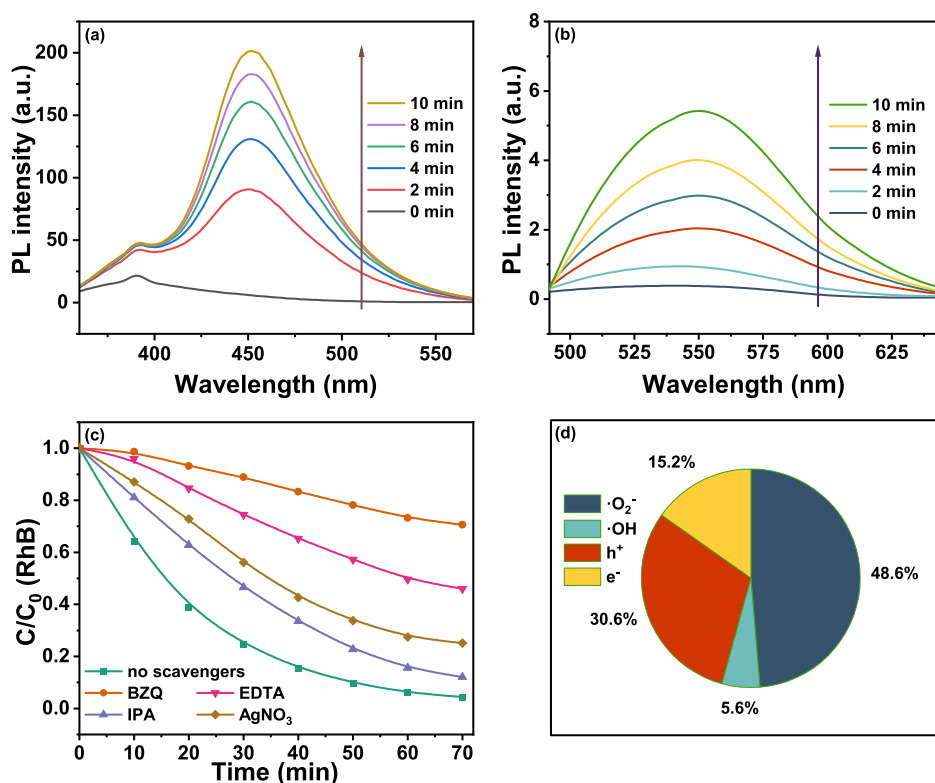


**Figure 18.** Fluorescence detection of  $\cdot\text{OH}$  (a) and  $\cdot\text{O}_2^-$  (b) for TC-3. The influence of active species scavengers on the degradation of RhB by TC-3 (c). Proportion of free radicals generated in the degradation of RhB by TC-3 (d).

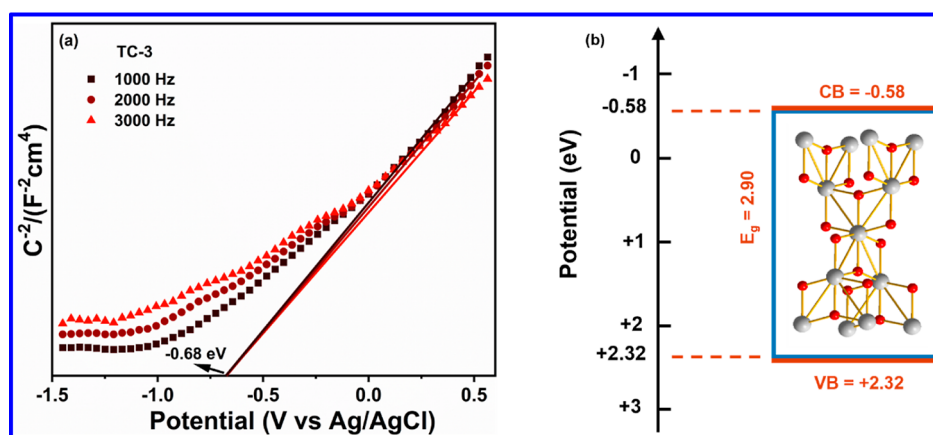


**Figure 19.** Mott–Schottky plot (a) and energy band schematic (b) of TC-3.

to TC-3, the degradation efficiency significantly decreased when EDTA and BZQ scavengers were added, indicating that  $\cdot\text{O}_2^-$  and  $\text{h}^+$  are the main active species in the degradation reaction. When IPA and  $\text{AgNO}_3$  were used as scavengers, the degradation efficiency also decreased, suggesting that  $\cdot\text{OH}$  and  $\text{e}^-$  had some influence on the reaction. Figure 18d displays the proportion of free radicals generated during the degradation of RhB in TC-3. The ratio of  $\cdot\text{OH}$ ,  $\text{e}^-$ ,  $\text{h}^+$ , and  $\cdot\text{O}_2^-$  generated by TC-3 within 70 min was approximately 1:2.7:5.5:8.7.

**3.11. Photocatalytic Mechanism.** Figure 19a shows the Mott–Schottky (MS) plot for TC-3, obtained using the formula  $C^{-2} = 2(V - V_{\text{FB}} - k_{\text{B}}T/e)/\epsilon\epsilon_0eN_{\text{D}}$ .<sup>62</sup> Here,  $C$ ,  $V$ ,  $V_{\text{FB}}$ ,  $k_{\text{B}}$ ,  $T$ ,  $e$ ,  $\epsilon$ ,  $\epsilon_0$ , and  $N_{\text{D}}$  represent the space charge capacitance, electrode potential, flat-band potential, Boltzmann constant, temperature, elementary charge, dielectric constant, vacuum

permittivity, and charge carrier density, respectively.  $V$  is the applied potential correction to  $\text{Ag}/\text{AgCl}$  of 0.197 eV.<sup>63</sup> A positive slope indicates that TC-3 was an n-type semiconductor, consistent with  $\text{TiO}_2$ . Furthermore, the  $V_{\text{FB}}$  potential of TC-3 was obtained by the intersection of the curve's tangent with the  $x$ -axis, which was  $-0.68$  eV compared to  $\text{Ag}/\text{AgCl}$  and  $-0.48$  eV compared to NHE. The voltage difference between the  $E_{\text{CB}}$  and  $V_{\text{FB}}$  for n-type semiconductors is typically between 0 and 0.2 V. Here, the voltage difference between  $E_{\text{CB}}$  and  $V_{\text{FB}}$  is 0.1 V.<sup>64</sup> According to calculations, the  $E_{\text{CB}}$  of TC-3 was  $-0.58$  V. Based on the formula  $E_{\text{VB}} = E_{\text{CB}} + E_{\text{g}}$ , where  $E_{\text{g}}$  is seen in Figure 7b, the  $E_{\text{VB}}$  of TC-3 was  $+2.32$  eV. The energy band of TC-3 is shown in Figure 19b.

In n-type semiconductors, there are two types of charge carriers:  $\text{h}^+$  in the valence band and  $\text{e}^-$  in the conduction band.

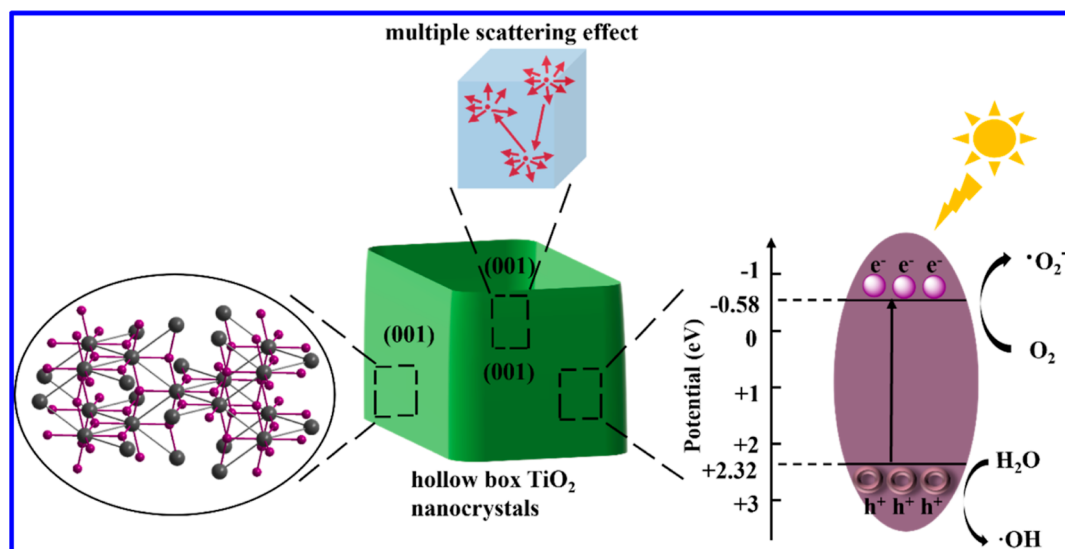
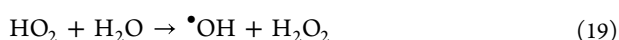
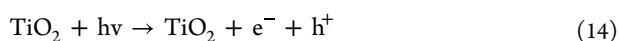


Figure 20. Photocatalytic mechanism of hollow box TiO<sub>2</sub> nanocrystals.

Hollow box TiO<sub>2</sub> nanocrystals generate e<sup>-</sup> and h<sup>+</sup> when exposed to sunlight. e<sup>-</sup> and h<sup>+</sup> can react with H<sub>2</sub>O, O<sub>2</sub>, and other substances. As shown in eqs 14–17, •OH and •O<sub>2</sub><sup>-</sup> are formed on the surface of TiO<sub>2</sub>. Additionally, generated •O<sub>2</sub><sup>-</sup> can further react to produce •OH, as shown in eqs 18–20. These active groups can reduce water to hydrogen gas and participate in redox reactions with organic pollutants on the surface of the catalyst.<sup>65</sup> Figure 20 is a schematic diagram illustrating the mechanism of photocatalytic reactions using hollow box TiO<sub>2</sub> nanocrystals. The multiscattering effect of the hollow box structure enhances the utilization of light by the catalyst. Compared to other crystal facets, the (001) crystal facet of TiO<sub>2</sub> has the highest surface energy (0.90 J/m<sup>2</sup>), which enhances the photocatalytic capability of TiO<sub>2</sub>.



**3.12. Analysis of (001) Facet Formation under Temperature Control.** Table 5 presents an analysis of the (001) facet exposure rate of TC-3 under temperature control. With increasing temperature, the (001) facet exposure rate of

Table 5. (001) Facet Exposure Ratios of TC-3 under Controlled Temperatures

sample	temperature (°C)	$\theta$ (deg)	$a$ (nm)	$b$ (nm)	(001) facets exposure ratio (%)
TC-3	180	71.57	279.7	288	84
	200	63.79	279.7	288	88
	220	46.16	279.7	288	92
	240	68.29	279.7	288	86

TC-3 initially rises and then declines. The highest (001) facet exposure rate of TC-3 was observed at a reaction temperature of 220 °C. This is because, as the temperature increases, the reaction rate accelerates. The stronger the influence of the structure-directing agent F within the molecule, the higher the (001) facet exposure rate rises. When the temperature exceeds 220 °C, the multilevel hollow box structure of TC-3 breaks down, resulting in a decrease in the (001) facet exposure rate. At the same time, a higher (001) facet exposure rate of TiO<sub>2</sub> corresponds to increased activity and improved photocatalytic performance. As shown in Figure 21a, during the preparation of hollow box TiO<sub>2</sub> nanocrystals, F acted as a structural orientation. The dihedral angle between the facets of the octahedron and the plane became smaller, and the exposure rate of the (001) crystal facet increased. There are two critical situations. When the dihedral angles are 90 and 0°, the exposure rates of the (001) crystal plane are 0 and 100%, respectively.

Figure 22a,b depicts Hirshfeld surface maps and fingerprint plots generated using Crystal Explorer 21.5. These were employed to visualize intermolecular interactions and calculate interatomic contacts within the crystal framework.<sup>66</sup> The blue and red regions represent low and high electron densities, respectively, due to short and long contacts between atoms. The white region indicates intermediate electron density, corresponding to contact points located at the van der Waals radii.<sup>67</sup> The contributions of Ti···F, F···Ti, Ti···O, and O···Ti (TiOF) were 7.6, 10.8, 19.9, and 14.6%, respectively, and the contributions of Ti···O and O···Ti (TiO<sub>2</sub>) were 28.0 and 28.9%, respectively. This indicated that the presence of F in the molecule had an impact on the formation of the (001) crystal facet of TiO<sub>2</sub>.

Hollow box TiO<sub>2</sub> nanocrystals were grown using four nucleation methods: the acid dissolution denucleation method, the topological phase transition method, the sonic solvothermal method, and the air atmosphere sintering method. Possible growth mechanisms were investigated, including the nucleation dissolution reaction, Oswald ripening, and hydrolysis. All four methods can produce complete hollow box structures, primarily composed of nanosheets with high exposed (001) crystal facets, enhancing the photocatalytic performance of

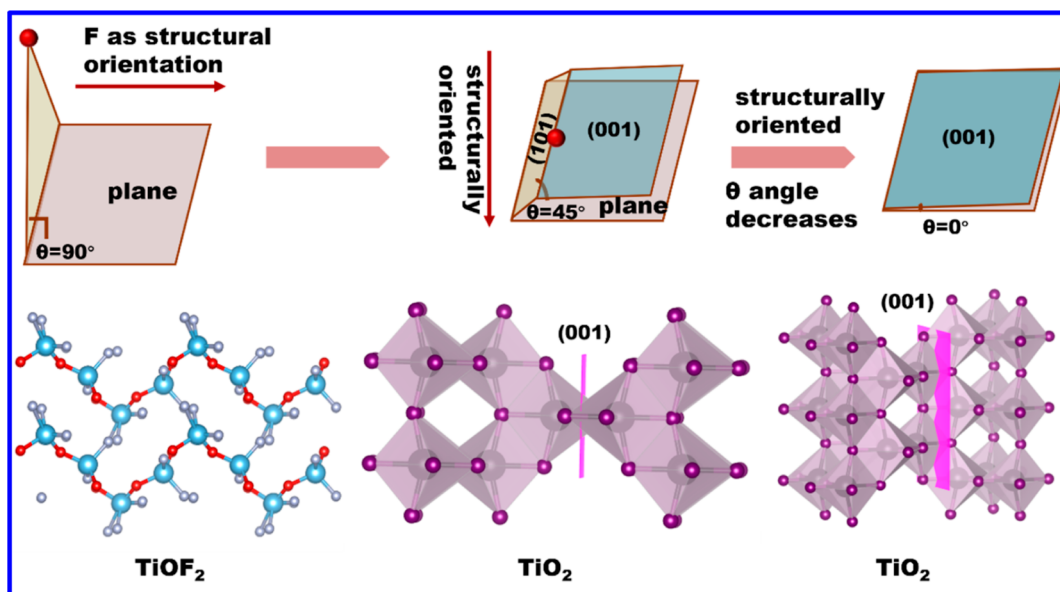


Figure 21. Relationship between the exposure rate of the (001) facet and the angle between the (101) facet and the reference plane.

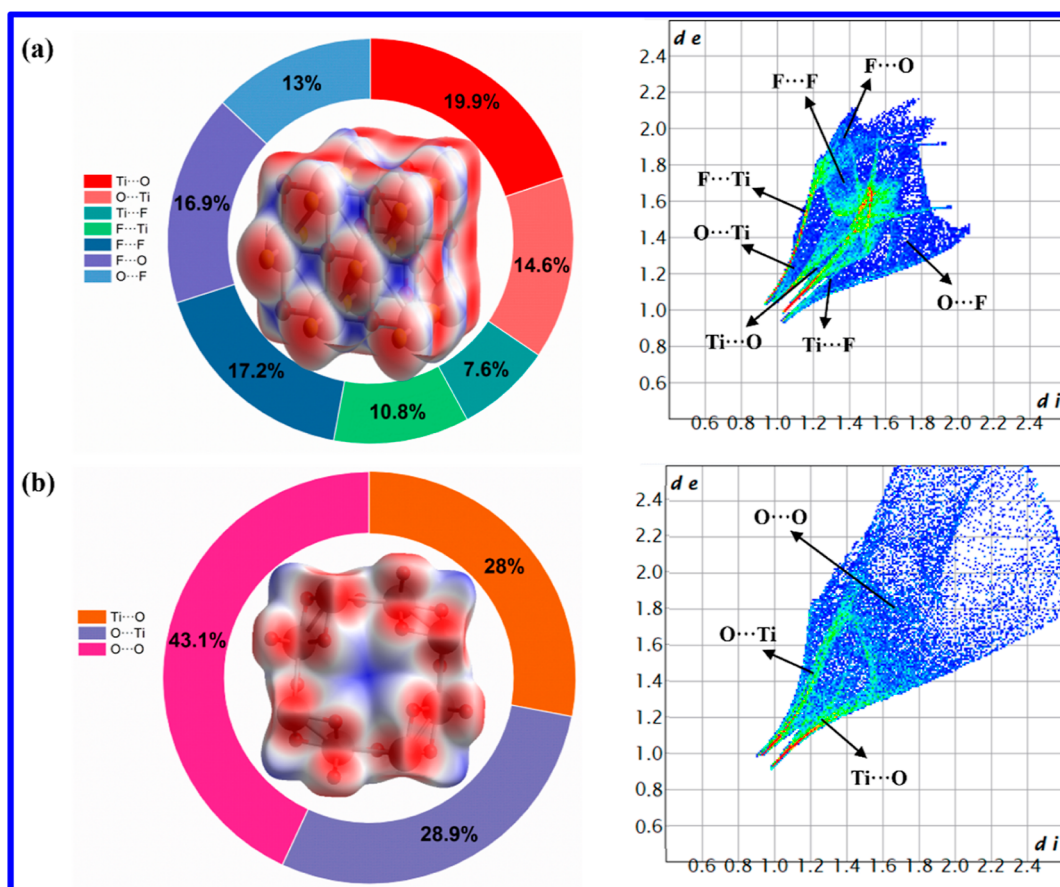


Figure 22.  $D_{\text{norm}}$  and fingerprint plots of TiOF (a) and TiO<sub>2</sub> (b).

TiO<sub>2</sub>. Calculations revealed that the (001) crystal facet exposed rates for TC-1, TC-2, TC-3, and TC-4 were 80, 87, 92, and 85%, respectively. It was found that the higher amount of water in the preparation conditions led to a lower exposed (001) crystal facet, which was related to the structural orientation of F. Photocatalytic performance studies were conducted under simulated sunlight irradiation, and TC-3

exhibited the best photocatalytic activity. TC-3 showed a hydrogen production rate of 93.88  $\mu\text{mol}/(\text{g h})$  and photocatalytic degradation rates of 96.59% for RhB and 75.25% for MB within 70 min. This was primarily attributed to the highly exposed (001) crystal facet and multilevel hollow box structure of TC-3. This study provides some references for growing highly active TiO<sub>2</sub> nanocrystals.

## AUTHOR INFORMATION

### Corresponding Author

**Lianqing Chen** – Key Laboratory of Catalysis and Energy Materials Chemistry of Ministry of Education & Hubei Key Laboratory of Catalysis and Materials Science, South-Central Minzu University, Wuhan 430074, China; Hubei Three Gorges Laboratory, Yichang 443000, China; Department of Chemistry, University of Wisconsin-Platteville, Platteville, Wisconsin 53818, United States; [orcid.org/0000-0003-3706-0683](https://orcid.org/0000-0003-3706-0683); Phone: +86-27-67842752; Email: [lqchen@mail.scuec.edu.cn](mailto:lqchen@mail.scuec.edu.cn)

### Authors

**Shengqiang Liao** – Key Laboratory of Catalysis and Energy Materials Chemistry of Ministry of Education & Hubei Key Laboratory of Catalysis and Materials Science, South-Central Minzu University, Wuhan 430074, China

**Huan Liu** – Key Laboratory of Catalysis and Energy Materials Chemistry of Ministry of Education & Hubei Key Laboratory of Catalysis and Materials Science, South-Central Minzu University, Wuhan 430074, China

**Yanfei Lu** – Key Laboratory of Catalysis and Energy Materials Chemistry of Ministry of Education & Hubei Key Laboratory of Catalysis and Materials Science, South-Central Minzu University, Wuhan 430074, China

**Chenglong Tang** – Key Laboratory of Catalysis and Energy Materials Chemistry of Ministry of Education & Hubei Key Laboratory of Catalysis and Materials Science, South-Central Minzu University, Wuhan 430074, China

**Benjun Xi** – Hubei Three Gorges Laboratory, Yichang 443000, China

Complete contact information is available at:

<https://pubs.acs.org/10.1021/acsomega.3c08300>

### Notes

The authors declare no competing financial interest.

## ACKNOWLEDGMENTS

This project was supported by the National Natural Science Foundation of China (21177161 and 52272102), the Hubei Province Excellent Talents Training Plan (RCJH15001), the Natural Science Foundation of Hubei Province for Distinguished Yong Scholars (2013CFA034), the Fundamental Research Funds for the Central University, South-Central Minzu University (CXY22006 and CZY23013), and the Open and Innovation Fund of Hubei Three Gorges Laboratory (SC232015).

## REFERENCES

- (1) Hens, Z.; De Roo, J. Atomically Precise Nanocrystals. *J. Am. Chem. Soc.* **2020**, *142* (37), 15627–15637.
- (2) Kojima, R.; Ogino, Y.; Naya, S.-i.; Soejima, T.; Tada, H. Seed-Assisted Hydrothermal Synthesis of Radial TiO<sub>2</sub> Homomocrystals and the Application as a Support for Plasmonic Photocatalysts. *Cryst. Growth Des.* **2023**, *23* (6), 4472–4479.
- (3) Vogt, C.; Weckhuysen, B. M. The Concept of Active Site in Heterogeneous Catalysis. *Nat. Rev. Chem.* **2022**, *6* (2), 89–111.
- (4) Yan, C.; Byrne, D.; Ondry, J. C.; Kahnt, A.; Moreno-Hernandez, I. A.; Kamat, G. A.; Liu, Z.-J.; Laube, C.; Crook, M. F.; Zhang, Y.; et al. Facet-selective Etching Trajectories of Individual Semiconductor Nanocrystals. *Sci. Adv.* **2022**, *8* (32), No. eabq1700.
- (5) Qin, C.; Jiang, Z.; Zhou, Z.; Liu, Y.; Jiang, Y. Multiexciton Dynamics in CsPbBr<sub>3</sub> Nanocrystals: The Dependence on Pump Fluence and Temperature. *Nanotechnology* **2021**, *32* (45), 455702.

- (6) Oh, M. H.; Cho, M. G.; Chung, D. Y.; Park, I.; Kwon, Y. P.; Ophus, C.; Kim, D.; Kim, M. G.; Jeong, B.; Gu, X. W.; et al. Design and Synthesis of Multigrain Nanocrystals Via Geometric Misfit Strain. *Nature* **2020**, *577* (7790), 359–363.

- (7) Keene, J. D.; Freymeyer, N. J.; McBride, J. R.; Rosenthal, S. J. Ultrafast Spectroscopy Studies of Carrier Dynamics in Semiconductor Nanocrystals. *iScience* **2022**, *25* (2), 103831.

- (8) Hu, X.; Zhang, T.; Jin, Z.; Huang, S.; Fang, M.; Wu, Y.; Zhang, L. Single-Crystalline Anatase TiO<sub>2</sub> Dots Assembled Micro-Sphere and Their Photocatalytic Activity. *Cryst. Growth Des.* **2009**, *9* (5), 2324–2328.

- (9) Rawool, S. A.; Yadav, K. K.; Polshettiwar, V. Defective TiO<sub>2</sub> for Photocatalytic CO<sub>2</sub> Conversion to Fuels and Chemicals. *Chem. Sci.* **2021**, *12* (12), 4267–4299.

- (10) Daraee, M.; Ghasemy, E.; Rashidi, A. Effective Adsorption of Hydrogen Sulfide by Intercalation of TiO<sub>2</sub> and N-doped TiO<sub>2</sub> in Graphene Oxide. *J. Environ. Chem. Eng.* **2020**, *8* (4), 103836.

- (11) Minnekhanov, A.; Kytina, E.; Konstantinova, E.; Kytin, V.; Marikutsa, A.; Elizarov, P. Photoinduced Dynamics of Radicals in N- and Nb-Codoped Titania Nanocrystals with Enhanced Photocatalysis: Experiment and Modeling. *Cryst. Growth Des.* **2022**, *22* (7), 4288–4297.

- (12) Gao, Z.; Zhao, Y.; Wang, H.; Wang, Y.; Jiang, L.; Xu, Y.; Xu, B.; Zheng, L.; Jin, C.; Liu, P.; et al. Rapid-Heating-Triggered in Situ Solid-State Transformation of Amorphous TiO<sub>2</sub> Nanotubes into Well-Defined Anatase Nanocrystals. *Cryst. Growth Des.* **2019**, *19* (2), 1086–1094.

- (13) Wang, L.; Chow, T. H.; Oppermann, M.; Wang, J.; Chergui, M. Giant Two-photon Absorption of Anatase TiO<sub>2</sub> in Au/TiO<sub>2</sub> Core-shell Nanoparticles. *Photonics Res.* **2023**, *11* (7), 1303.

- (14) Comarmond, M. J.; Payne, T. E.; Harrison, J. J.; Thiruvoth, S.; Wong, H. K.; Aughterson, R. D.; Lumpkin, G. R.; Müller, K.; Föersterndorf, H. Uranium Sorption on Various Forms of Titanium Dioxide – Influence of Surface Area, Surface Charge, and Impurities. *Environ. Sci. Technol.* **2011**, *45* (13), 5536–5542.

- (15) Chen, Z.; Chen, H.; Wang, K.; Chen, J.; Li, M.; Wang, Y.; Tsiakaras, P.; Song, S. Enhanced TiO<sub>2</sub> Photocatalytic 2 e<sup>-</sup> Oxygen Reduction Reaction via Interfacial Microenvironment Regulation and Mechanism Analysis. *ACS Catal.* **2023**, *13* (10), 6497–6508.

- (16) Tayade, R. J.; Surolia, P. K.; Kulkarni, R. G.; Jasra, R. V. Photocatalytic Degradation of Dyes and Organic Contaminants in Water Using Nanocrystalline Anatase and Rutile TiO<sub>2</sub>. *Sci. Technol. Adv. Mater.* **2007**, *8* (6), 455–462.

- (17) Li, G.; Huang, J.; Deng, Z.; Chen, J.; Huang, Q.; Liu, Z.; Guo, W.; Cao, R. Highly Active Photocatalyst of CuO<sub>x</sub> Modified TiO<sub>2</sub> Arrays for Hydrogen Generation. *Cryst. Growth Des.* **2019**, *19* (10), 5784–5790.

- (18) Zhu, J.; Chen, J.; Zhuang, P.; Zhang, Y.; Wang, Y.; Tan, H.; Feng, J.; Yan, W. Efficient Adsorption of Trace Formaldehyde by Polyaniline/TiO<sub>2</sub> Composite at Room Temperature and Mechanism Investigation. *Atmos. Pollut. Res.* **2021**, *12* (2), 1–11.

- (19) Yang, P.; Guo, H.; Wu, H.; Zhang, F.; Liu, J.; Li, M.; Yang, Y.; Cao, Y.; Yang, G.; Zhou, Y. Boosting Charge-transfer in Tuned Au Nanoparticles on Defect-rich TiO<sub>2</sub> Nanosheets for Enhancing Nitrogen Electroreduction to Ammonia Production. *J. Colloid Interface Sci.* **2023**, *636*, 184–193.

- (20) Xu, S.; Zhang, Y.; Hardacre, C.; Liu, Z. Enhanced Catalytic Activity of Pd Supported on TiO<sub>2</sub> Nanowire for the H<sub>2</sub>-SCR of NO<sub>x</sub> in the Presence of Oxygen. *ACS Sustain. Chem. Eng.* **2023**, *11* (28), 10453–10461.

- (21) Zhang, K.; Zhang, Y.; Liu, S.; Tong, X.; Niu, J.; Wang, D.; Yan, J.; Xiong, Z.; Crittenden, J. Influence of MnO<sub>x</sub> Deposition on TiO<sub>2</sub> Nanotube Arrays for Electrooxidation. *Green Energy Environ.* **2023**, *8* (2), 612–618.

- (22) Li, S.; Shuler, E. W.; Willinger, D.; Nguyen, H. T.; Kim, S.; Kang, H. C.; Lee, J.-J.; Zheng, W.; Yoo, C. G.; Sherman, B. D.; et al. Enhanced Photocatalytic Alcohol Oxidation at the Interface of RuC-Coated TiO<sub>2</sub> Nanorod Arrays. *ACS Appl. Mater. Interfaces* **2022**, *14* (20), 22799–22809.

- (23) Zhang, B.; Li, D.; Xiong, W.; Wu, M.; Chu, B.; Liu, H.; Huang, M.; Fan, M.; Li, B.; Dong, L. Fabrication of Three-dimensional Hollow Nanocassette Photocatalysts RE-TiO<sub>2</sub> (RE = La, Ce, Sm, Yb, and Tm) with Enhanced Pesticide Degradation Activity and Highly Exposed (1 0 1) Crystal Planes. *Appl. Surf. Sci.* **2023**, *626*, 157239.
- (24) Wang, Y.; Zhang, Y.; Zhu, X.; Liu, Y.; Wu, Z. Fluorine-induced Oxygen Vacancies on TiO<sub>2</sub> Nanosheets for Photocatalytic Indoor VOCs Degradation. *Appl. Catal., B* **2022**, *316*, 121610.
- (25) Horváth, E.; Gabathuler, J.; Bourdieu, G.; Vidal-Revel, E.; Benthem Muñiz, M.; Gaal, M.; Grandjean, D.; Breider, F.; Rossi, L.; Sienkiewicz, A.; et al. Solar Water Purification with Photocatalytic Nanocomposite Filter Based on TiO<sub>2</sub> Nanowires and Carbon Nanotubes. *npj Clean Water* **2022**, *5* (1), 10.
- (26) Yang, H. G.; Sun, C. H.; Qiao, S. Z.; Zou, J.; Liu, G.; Smith, S. C.; Cheng, H. M.; Lu, G. Q. Anatase TiO<sub>2</sub> Single Crystals with a Large Percentage of Reactive Facets. *Nature* **2008**, *453* (7195), 638–641.
- (27) Chen, Y.; Li, W.; Wang, J.; Gan, Y.; Liu, L.; Ju, M. Microwave-assisted Ionic Liquid Synthesis of Ti<sup>3+</sup> Self-doped TiO<sub>2</sub> Hollow Nanocrystals with Enhanced Visible-light Photoactivity. *Appl. Catal., B* **2016**, *191*, 94–105.
- (28) Liu, G.; Li, W.; Bi, R.; Atangana Etogo, C.; Yu, X.-Y.; Zhang, L. Cation-Assisted Formation of Porous TiO<sub>2-x</sub> Nanoboxes with High Grain Boundary Density as Efficient Electrocatalysts for Lithium–Oxygen Batteries. *ACS Catal.* **2018**, *8* (3), 1720–1727.
- (29) Wu, Y.-H.; Cao, Y.-F.; Fu, Z.-Z.; Lei, B.-X.; Sun, Z.-F. Cube-like Mixed-phases TiO<sub>2</sub> Mesocrystalline Hollow Boxes from In Situ Topotactic Transformation for Highly Efficient Dye-Sensitized Solar Cells. *Adv. Powder Technol.* **2021**, *32* (1), 186–193.
- (30) Liu, S.-J.; Wu, X.-X.; Hu, B.; Gong, J.-Y.; Yu, S.-H. Novel Anatase TiO<sub>2</sub> Boxes and Tree-like Structures Assembled by Hollow Tubes: d,l-Malic Acid-Assisted Hydrothermal Synthesis, Growth Mechanism, and Photocatalytic Properties. *Cryst. Growth Des.* **2009**, *9* (3), 1511–1518.
- (31) Guo, F.; Huang, X.; Chen, Z.; Shi, Y.; Sun, H.; Cheng, X.; Shi, W.; Chen, L. Formation of Unique Hollow ZnSnO<sub>3</sub>@ZnIn<sub>2</sub>S<sub>4</sub> Core-shell Heterojunction to Boost Visible-light-driven Photocatalytic Water Splitting for Hydrogen Production. *J. Colloid Interface Sci.* **2021**, *602*, 889–897.
- (32) Liu, B.; Li, X.; Zhao, Q.; Hou, Y.; Chen, G. Self-templated Formation of ZnFe<sub>2</sub>O<sub>4</sub> Double-shelled Hollow Microspheres for Photocatalytic Degradation of Gaseous O-dichlorobenzene. *J. Mater. Chem. A* **2017**, *5* (19), 8909–8915.
- (33) Zhang, C.; Tian, L.; Chen, L.; Li, X.; Lv, K.; Deng, K. One-pot Topotactic Synthesis of Ti<sup>3+</sup> Self-Doped 3D TiO<sub>2</sub> Hollow Nanoboxes with Enhanced Visible Light Response. *Chin. J. Catal.* **2018**, *39* (8), 1373–1383.
- (34) Li, C.; He, K.; Sun, W.; Wang, B.; Yu, S.; Hao, C.; Chen, K. Synthesis of Hollow TiO<sub>2</sub> Nanobox with Enhanced Electrorheological Activity. *Ceram. Int.* **2020**, *46* (10), 14573–14582.
- (35) Cha, H.; Wu, A.; Kim, M.-K.; Saigusa, K.; Liu, A.; Miljkovic, N. Nanoscale-Agglomerate-Mediated Heterogeneous Nucleation. *Nano Lett.* **2017**, *17* (12), 7544–7551.
- (36) Xiao, J.; Xiao, N.; Li, K.; Zhang, L.; Chang, J.; Ma, X.; Li, H.; Bai, J.; Jiang, Q.; Qiu, J. Ultra-High Fluorine Enhanced Homogeneous Nucleation of Lithium Metal on Stepped Carbon Nanosheets with Abundant Edge Sites. *Adv. Energy Mater.* **2022**, *12* (10), 2103123.
- (37) Wlasits, P. J.; Konrat, R.; Winkler, P. M. Heterogeneous Nucleation of Supersaturated Water Vapor onto Sub-10 nm Nanoplastic Particles. *Environ. Sci. Technol.* **2023**, *57* (4), 1584–1591.
- (38) Hussain, S.; Haji-Akbari, A. How to Quantify and Avoid Finite Size Effects in Computational Studies of Crystal Nucleation: The Case of Homogeneous Crystal Nucleation. *J. Chem. Phys.* **2022**, *156* (5), 054503.
- (39) Su, M.; Shi, J.; Kang, Q.; Lai, D.; Lu, Q.; Gao, F. One-step Multiple Structure Modulations on Sodium Vanadyl Phosphate@Carbon Towards Ultra-stable High Rate Sodium Storage. *Chem. Eng. J.* **2022**, *432*, 134289.
- (40) Wu, Z.; Zhao, Y.; Mi, L.; Guo, Y.; Wang, H.; Liu, K.; Zhang, K.; Wang, B. Preparation of g-C<sub>3</sub>N<sub>4</sub>/TiO<sub>2</sub> by Template Method and Its Photocatalytic Performance. *Colloids Surf., A* **2021**, *624*, 126756.
- (41) Zhu, Q.; Chang, X.; Sun, N.; Chen, R.; Zhao, Y.; Xu, B.; Fu, F. Confined Growth of Nano-Na<sub>3</sub>V<sub>2</sub>(PO<sub>4</sub>)<sub>3</sub> in Porous Carbon Framework for High-Rate Na-Ion Storage. *ACS Appl. Mater. Interfaces* **2019**, *11* (3), 3107–3115.
- (42) Chiba, Y.; Oka, Y.; Masai, H.; Matsuda, W.; Fujihara, T.; Tsuji, Y.; Terao, J. Two-step Template Method for Synthesis of Axis-length-controlled Porphyrin-containing Hollow Structures. *Chem. Commun.* **2019**, *55* (47), 6755–6758.
- (43) Yang, T.; Liu, Y.; Xia, G.; Zhu, X.; Zhao, Y. Degradation of Formaldehyde and Methylene Blue Using Wood-templated Biomimetic TiO<sub>2</sub>. *J. Cleaner Prod.* **2021**, *329*, 129726.
- (44) Zhu, B.; Xu, J.; Xu, Z.; Wu, M.; Jiang, H. Soft-template Solvent Thermal Method Synthesis of Magnetic Mesoporous Carbon–Silica Composite for Adsorption of Methyl Orange from Aqueous Solution. *Environ. Sci. Pollut. Res.* **2022**, *29* (27), 40734–40744.
- (45) Kominami, H.; Kohno, M.; Matsunaga, Y.; Kera, Y. Thermal Decomposition of Titanium Alkoxide and Silicate Ester in Organic Solvent: A New Method for Synthesizing Large-Surface-Area, Silica-Modified Titanium(IV) Oxide of High Thermal Stability. *J. Am. Ceram. Soc.* **2001**, *84* (5), 1178–1180.
- (46) Jia, C.; Kan, X.; Zhang, X.; Lin, G.; Liu, W.; Wang, Z.; Zhu, S.; Ju, D.; Liu, J. Construction of Frustrated Lewis Pairs on TiO<sub>2-x</sub> Derived from Perovskite for Enhanced Photocatalytic CO<sub>2</sub> Reduction. *Chem. Eng. J.* **2022**, *427*, 131554.
- (47) Pei, W.; Zhao, D.; Chen, X.; Wang, X.; Yang, X.; Wang, J.; Li, Z.; Zhou, L. Evolution of the Phases and the Polishing Performance of Ceria-based Compounds Synthesized by a Facile Calcination Method. *RSC Adv.* **2019**, *9* (46), 26996–27001.
- (48) Hamzah, M. S.; Wildan, M. W.; Kusmono; Suharyadi, E. Effect of Sintering Temperature on Physical, Mechanical, and Electrical Properties of Nano Silica Particles Synthesized from Indonesia Local Sand for Piezoelectric Application. *J. Asian Ceram. Soc.* **2023**, *11* (1), 178–187.
- (49) Sarbishei, S.; Tafaghodi Khajavi, L. Kinetic Analysis on Nickel Laterite Ore Calcination Using Model-free and Model-fitting Methods. *Miner. Eng.* **2019**, *136*, 129–139.
- (50) Gao, W.; Zhang, B.; Xiang, F. Effect of Sintering Atmosphere and Annealing Temperature on Electrical and Optical Properties of TiO<sub>2</sub> Ceramic. *J. Mater. Sci.: Mater. Electron.* **2020**, *31* (16), 13857–13861.
- (51) Maleki, F.; Pacchioni, G. Iso-valent Doping of Reducible Oxides: a Comparison of Rutile (110) and Anatase (101) TiO<sub>2</sub> Surfaces. *J. Phys. Condens. Matter.* **2021**, *33* (49), 494001.
- (52) Zhao, X.; Du, Y.; Zhang, C.; Tian, L.; Li, X.; Deng, K.; Chen, L.; Duan, Y.; Lv, K. Enhanced Visible Photocatalytic Activity of TiO<sub>2</sub> Hollow Boxes Modified by Methionine for RhB Degradation and NO Oxidation. *Chin. J. Catal.* **2018**, *39* (4), 736–746.
- (53) Lee, S. M.; Park, G. C.; Seo, T. Y.; Jung, S.-B.; Lee, J. H.; Kim, Y. D.; Choi, D. H.; Lim, J. H.; Joo, J. Facet-controlled Anatase TiO<sub>2</sub> Nanoparticles through Various Fluorine Sources for Superior Photocatalytic Activity. *Nanotechnology* **2016**, *27* (39), 395604.
- (54) Hu, C.; Lian, C.; Zheng, S.; Li, X.; Lu, T.; Hu, Q.; Duo, S.; Zhang, R.; Sun, Y.; Chen, F. Improved Photocatalytic Activity of TiO<sub>2</sub> Produced by an Alcohothermal Approach through in-Situ Decomposition of NH<sub>4</sub>HCO<sub>3</sub>. *J. Energy Chem.* **2016**, *25* (3), 489–494.
- (55) Zeng, X.; Yang, W.; Song, F. X.; Wang, H. X.; Li, Y. Preparation of Functionalized Redox Response Type TiO<sub>2</sub>&SiO<sub>2</sub> Nanomaterials and Research on Anti-Tumor Performance. *J. Drug Delivery Sci. Technol.* **2022**, *68*, 103120.
- (56) Palomino-Merino, R.; Trejo-Garcia, P.; Portillo-Moreno, O.; Jiménez-Sandoval, S.; Tomás, S.; Zelaya-Angel, O.; Lozada-Morales, R.; Castaño, V. Red Shifts of the Eg(1) Raman Mode of Nanocrystalline TiO<sub>2</sub>:Er Monoliths Grown by Sol–gel process. *Opt. Mater.* **2015**, *46*, 345–349.
- (57) Zhu, J.; Yang, D.; Geng, J.; Chen, D.; Jiang, Z. Synthesis and Characterization of Bamboo-like CdS/TiO<sub>2</sub> Nanotubes Composites

with Enhanced Visible-light Photocatalytic Activity. *J. Nanopart. Res.* **2008**, *10* (5), 729–736.

(58) Nguyen, D. T.; Kim, K.-S. Self-Development of Hollow TiO<sub>2</sub> Nanoparticles by Chemical Conversion Coupled with Ostwald Ripening. *Chem. Eng. J.* **2016**, *286*, 266–271.

(59) Cao, Y.; Zong, L.; Li, Q.; Li, C.; Li, J.; Yang, J. Solvothermal Synthesis of TiO<sub>2</sub> Nanocrystals with {001} Facets Using Titanic Acid Nanobelts for Superior Photocatalytic Activity. *Appl. Surf. Sci.* **2017**, *391*, 311–317.

(60) Huang, Z. a.; Wang, Z.; Lv, K.; Zheng, Y.; Deng, K. Transformation of TiOF<sub>2</sub> Cube to a Hollow Nanobox Assembly from Anatase TiO<sub>2</sub> Nanosheets with Exposed {001} Facets via Solvothermal Strategy. *ACS Appl. Mater. Interfaces* **2013**, *5* (17), 8663–8669.

(61) Yan, A.; Shi, X.; Huang, F.; Fujitsuka, M.; Majima, T. Efficient Photocatalytic H<sub>2</sub> Evolution Using NiS/ZnIn<sub>2</sub>S<sub>4</sub> Heterostructures with Enhanced Charge Separation and Interfacial Charge Transfer. *Appl. Catal., B* **2019**, *250*, 163–170.

(62) Pan, J.; Dong, Z.; Wang, B.; Jiang, Z.; Zhao, C.; Wang, J.; Song, C.; Zheng, Y.; Li, C. The Enhancement of Photocatalytic Hydrogen Production via Ti<sup>3+</sup> Self-doping Black TiO<sub>2</sub>/g-C<sub>3</sub>N<sub>4</sub> Hollow Core-shell Nano-heterojunction. *Appl. Catal., B* **2019**, *242*, 92–99.

(63) Hu, Z.; Zhou, M.; Maitlo, H. A.; Liang, R.; Zheng, Y.; Wu, H.; Song, X.; Arotiba, O. A. Novel Dual-photoelectrode Photoelectrocatalytic System Based on TiO<sub>2</sub> Nanoneedle Arrays Photoanode and Nitrogen-doped Carbon Dots/Co<sub>3</sub>O<sub>4</sub> Photocathode for Efficient Water Purification at Low/no Applied Voltage. *Appl. Catal., B* **2023**, *331*, 122676.

(64) Huang, M.; Zhang, S.; Wu, B.; Yu, X.; Gan, Y.; Lin, T.; Yu, F.; Sun, Y.; Zhong, L. Highly Selective Photocatalytic Aerobic Oxidation of Methane to Oxygenates with Water over W-doped TiO<sub>2</sub>. *ChemSusChem* **2022**, *15* (14), No. e202200548.

(65) Hwang, J. Y.; Moon, G.-h.; Kim, B.; Tachikawa, T.; Majima, T.; Hong, S.; Cho, K.; Kim, W.; Choi, W. Crystal Phase-dependent Generation of Mobile OH Radicals on TiO<sub>2</sub>: Revisiting the Photocatalytic Oxidation Mechanism of Anatase and Rutile. *Appl. Catal., B* **2021**, *286*, 119905.

(66) Yue, Z.-Y.; Xiang, L.; Wang, N.; Zou, L.-L.; Miao, L.-P.; Ye, H.-Y.; Shi, C. Series of Cage-Like Double Perovskite-Type Hybrid Perovskites with Reversible Structural Phase Transition and Switchable Dielectric Constant Property. *Cryst. Growth Des.* **2023**, *23* (9), 6860–6865.

(67) Clausen, H. F.; Chevallier, M. S.; Spackman, M. A.; Iversen, B. B. Three New Co-crystals of Hydroquinone: Crystal Structures and Hirshfeld Surface Analysis of Intermolecular Interactions. *New J. Chem.* **2010**, *34* (2), 193–199.